Experimental investigation on an air tubular absorber enhanced with Raschig Rings porous medium in a solar furnace

Applied Energy 342 (2023) 121189

Contents lists available at ScienceDirect

Applied Energy

journal homepage: www.elsevier.com/locate/apenergy

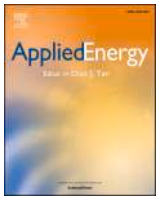

Experimental investigation on an air tubular absorber enhanced with Raschig Rings porous medium in a solar furnace

Hossein Ebadi [a], Antonio Cammi [b], Rosa Difonzo [a], José Rodríguez [c], Laura Savoldi [a,*]

[a] MAHTEP Group, Dipartimento Energia "Galileo Ferraris" (DENERG), Politecnico di Torino, Italy
[b] Department of Energy, Politecnico di Milano, Italy
[c] CIEMAT-Plataforma Solar de Almeria, 04200 Tabernas, Almeria, Spain

HIGHLIGHTS

- Two tubular receivers with Raschig Rings porous inserts are tested at a solar Furnace.
- Effects of coating, porous length, airflow rate, solar flux on thermal performance are analyzed.
- The porous inserts improve the energy efficiency by 30–50%.
- The porous inserts enhance the exergy efficiency by 61–73%.

ARTICLE INFO

Keywords:
CSP
Porous insert
Solar furnace
Raschig Rings
Exergy

ABSTRACT

An experimental study was carried out to assess the performance of a tubular absorber enhanced with Raschig Rings (RR) porous medium for CSP applications. Two alternative designs with different porous lengths of 20 and 40 mm were fabricated and compared with two conventional tube designs with and without surface coating. Several tests were conducted at the solar furnace SF60 of the Plataforma Solar de Almería (PSA) within the international access program of the SFERA III project, financed by the EU. The main scope of the study was to provide comprehensive detail on the hydraulic and thermal characteristics of the modified tube for further optimization and deployment in point-focusing solar systems. Therefore, evaluations were directed to determine the effects of each design on the pressure losses and the tube wall temperature, as well as on the useful heat gain. Results indicated that although the porous inserts rise the pressure losses through the fluid flow, the higher wetted area in the porous zone for heat transfer between the air and the heated plate reduces the wall temperature significantly. Moreover, applying the PYROMARK 2500 as the surface coating has a high influence on increasing solar absorption and reducing thermal losses. Further investigations revealed that the integration of the porous medium changes the temperature profile formed all over the tube, transforming a Gaussian shape in the plain pipes to a spline shape with two peaks in the modified tubes. Increasing the energy and exergy efficiencies of the solar absorber up to 30–50% and 60–70%, respectively, demonstrated the improving effects of the proposed porous material for future applications in the solar industry.

1. Introduction

Concentrating solar power (CSP) technology is becoming a robust alternative to conventional fossil fuels in the context of the energy transition. Thanks to the recent technological advances, it is believed that by 2030 CSP continues its current falling trends in the Levelized Cost of Electricity (LCE), hitting a 35% reduction compared to 2018, and reaching USD 0.086 per kWh (IRENA 2020 [1]). According to the latest data (2021) [2], the global capacity of power produced by CSP has gained nearly 6.4 GW with 135 operational power plants [3]. One of the promising point-focusing systems is the Solar Power Towers (SPT) which stands second with 15% of total CSP power generation after 80% of Parabolic Trough Collectors (PTC) [4]. Billboard receivers are among the most disseminated designs in SPT, which usually are formed as a panel consisting of several tubular receivers connected together [5].

According to the advances in material science, a variety of Heat

* Corresponding author.
E-mail address: laura.savoldi@polito.it (L. Savoldi).

https://doi.org/10.1016/j.apenergy.2023.121189
Received 7 November 2022; Received in revised form 17 January 2023; Accepted 21 April 2023
Available online 5 May 2023

Transfer Fluids (HTF) have been used and validated in solar CSP systems, where a broad classification was made by Benoit et al. [6], introducing liquid, gaseous, two-phase, and particle-based fluids. Based on the comparison made by Vutukuru [7] to assess the suitability of different fluids for high-temperature solar systems, when the gaseous HTFs are employed, the area ratios (a function of ratios of heat transfer coefficient of gaseous and liquid HTFs) and diameter ratios (a function of ratios of specific heat capacity, density, and viscosity of gaseous and liquid HTFs) are smaller for the gaseous HTFs, with respect to the liquid HTFs. This brings overall lower volume ratios, leading to lighter and cheaper solar systems [7]. Bellos et al. [8] proved that gaseous PTC absorbers could be the ideal options for extremely high-temperature levels (above 1100 K) and their exergy efficiency can reach up to 42%, similar to that obtained by liquid fluids. The other aspects that put the air receivers in front are the availability of the fluid, no need for trace heating, non-toxicity, and a 3–5 h of thermal storage ability due to the volumetric effect that brings higher-efficiency thermodynamic cycles [9].

The role of gaseous receivers in SPT technology is in a wide range of applications. Neber and Lee [10] proposed a new modular cavity air absorber to be applied to dish-Brayton systems, working at a small scale and for residential use. Utilizing the high absorptivity and conductivity of silicon carbide, they developed a cavity receiver with a tube-style heat exchanger embedded inside to have lower pressure drops and higher efficiency compared to ceramic foams. Testing the absorber in a parabolic dish collector and using air as the HTF, the experimental results showed that the outlet temperature could reach $>$ 1200 K. In another study [11], the air was investigated with a volumetric receiver, consisting of a series of squared-shaped cups for SPT technologies. The employment of a multi-scale analysis approach let the researchers investigate the effects of operating parameters on the performance at different scales and further predict the absorber behavior under the transient scenario. Chen et al. [12] studied the use of supercritical CO_2 (sCO_2) as the HTF in a conical absorber consisting of a coiled tube integrated with a solar parabolic dish. Conducting a thermo-mechanical numerical investigation using FVM and FEM methods, they studied both the influences of geometric and operation parameters. Cagnoli et al. [13] combined optical and CFD analyses to conduct a parametric study on the thermal performance of an open volumetric solar air receiver of honeycomb type (multiple parallel channels). As a result, a new criterion was introduced as the overall (solar-to-electricity) efficiency, which includes both the receiver efficiency and the influence of the air outlet temperature on the efficiency of the power unit.

However, the heat transfer capacity is one of the challenges associated with gaseous absorbers, where air with a 10 bar operating pressure has still a heat transfer lower by one or two orders of magnitude compared to thermal oils, and this highlights the importance of additional enhancers in air-based systems [6]. Works reporting the thermal enhancement of high-temperature gaseous absorbers are not abundant and those published are categorized based on the absorber designs. In the case of tubular receivers, the integration of flow inserts and porous media are the two main techniques used for the aims of reduction in thermal boundary layer thickness, improving the heat transfer area, and enhancing turbulence in the fluid region could be some of the options for tubular solar gaseous receivers [14]. In an experiment carried out by Cantone et al. [15] two turbulence promoters were associated with a tubular receiver to assess its performance in a solar furnace. Both numerical and experimental analyses revealed that the tubes with helical ribs and the annual rings could enhance the total useful power by respectively $>$ 30% and $>$ 25% compared to the conventional tube. Furthermore, considering both the penalty in pumping power and the augmentation of the Nusselt number, the best thermal enhancement factor was obtained as $\sim$ 1.4 for the helically ribbed tube at a flow rate of 38 L/min. Ahmed and Natarajan [16] numerically investigated the effects of toroidal rings in an absorber tube of a solar parabolic trough collector using gaseous HTF. Results indicated that the optimum ratio of the inner to the outer diameter of the toroidal ring is 0.90 for the highest exergy efficiency, reaching $>$ 40% when helium is used as the heat transfer medium. Bellos et al. [17] developed a numerical simulation for a tubular receiver with internal longitudinal fins used in PTC technology with various gaseous fluids. They reported that the best fin length to tube inner diameter ratio must be 0.15 to attain the highest exergy efficiency and helium is the most favorable gas for operating temperatures up to 290 °C, while carbon dioxide is a better option for temperatures above this limit. In another study, Nems and Kasperski [18] experimentally investigated the performance of a novel solar PTC air heater with an internal multiple-fin array and later expanded their work [19] to compare a range of internal fin configurations. The integration of the numerical methods let the researchers find the plausibility of the fin-array technology with a 14% improvement of the efficiency in relation to the smooth pipe arrangement for the solar collector with black paint and a double glass envelope. Moreover, it was found that the insertion of such fins could reduce the needed air flux by 7–10 times compared to the smooth pipe arrangement of the absorber to get the same useful power to the fluid.

One of the simple techniques which requires the lowest surface modification is the insertion of a porous medium in the tubular receivers to improve the thermal performance of the system. Reddy and Satyanarayana [20] developed a numerical model for a parabolic trough collector enhanced with stainless steel porous fins (porosity = 0.37) using Therminol VP1 as the HTF. Optimization results stated that the integration of trapezoidal porous fins brings the highest heat transfer coefficient, resulting in a lower heat loss with a moderate pressure drop penalty. In the other work, Kumar and Reddy [21] tested numerically various stainless steel porous discs with a range of porosity (0.1–0.6) for a liquid-based PTC receiver and reported that the increments in heat transfer rate are $>$ 13% and $>$ 30% for respectively, water and Therminol oil-55 with a moderate pumping power penalty. In a further study, Reddy et al. [22] conducted an experimental investigation on their enhanced metallic porous discs (porosity = 0.3 and 0.5) with a 15 m^2 solar parabolic trough collector and found an increase in the collector efficiency with a moderate increase in pumping power with respect to total pumping power without the porous insert. Zheng et al. [23] studied the effects of partial-filling of porous inserts made of steel, silicon carbide, and copper in a solar central receiver tube for a variety of porosity, working under non-uniform heating conditions with liquid-phase HTFs and asserted that the porous inserts are a useful tool to avoid hotspots on the solar STP receivers. Moreover, the thermal conductivity ratio (thermal conductivity of porous medium over that of working fluid) was pointed out as a key factor in reaching reasonable thermo-hydraulic behavior. The utilization of a copper foam with a porosity of 0.9 was tested by Jamal-Abad et al. [24] for a small-scale PTC, using water as the heat transfer medium. Results revealed that when the absorber is filled with porous foam, the overall thermal loss coefficient decreases by 45% while the heat removal factor reduces slightly.

The application of porous technology with gaseous solar absorbers (tubular and rectangular) is not new and the literature [25,26] embodies numerous examples of low-temperature collectors equipped with porous inserts. However, the number of works concerning CSP applications is scarce and still suffers from gaps in knowledge, especially for SPT systems [27]. Jamal-Abad et al. [28] conducted a parametric study on heat transfer of an air-based PTC system using the perturbation technique. Applying the Brinkmane-Forchheimer equation to study the flow through the porous medium led the scientists to investigate the effects of shape and radiation parameters on the collector efficiency and heat removal factor. In the following, Savoldi et al. [29] performed one of the primary experiments on the dissemination of air rectangular-shaped receivers in CSP with porous inserts, using a planar mock-up. The authors tried to adopt copper mm-size Raschig Rings (RR) as the main element in a novel porous medium through a brazing process. According to the experimental and numerical data, it was found that the insertion of RR porous medium below the heated side allows the maximum

surface temperature to significantly decrease, with a nearly 5 times higher Nu number, with respect to a plain channel with the same envelope. RRs are small hollow cylinders that are used in different sizes for a broad spectrum of applications ranging from chemical to environmental industries [30]. They are mainly used for their large surface in the heat removal process from high heat flux components such as the resonant cavity of MW-class gyrotron [31], where they are mainly adopted for their heat transfer enhancement capability [32]. Moreover, the use of RR catalysts as a part of the reactor fill has shown a remarkable ability to reduce the pressure drop over the reactor, compared to other fillings such as cylinders and spheres [33].

This work conceptualizes the above-mentioned features as performance enhancement drivers, providing the analysis of a similar structure (hollow cylindrical container with a packed bed of RR) in the format of a porous matrix inserted inside an absorber tube. The work presented here aims at investigating experimentally the effects of the RR porous insert on the thermo-hydraulic performance of an air tubular receiver in STP systems. Prior to this study, a numerical study [34] was conducted by the authors to examine the feasibility of the RR integration with tubular receivers and the results proved the excellent ability of such technology in thermal efficiency enhancements. Based on that, this study provides a comprehensive experimental analysis of the application of RR porous inserts within air tubes used in the solar furnace at the Plataforma Solar de Almeria and studies the effects of the PYROMARK coating, two tube lengths and different operating parameters such as airflow rate and solar flux on the thermal performance.

2. Material and methods

2.1. Modified solar absorber

As shown in Fig. 1a, a conventional 316L stainless-steel tube was chosen as the basic solar absorber, in which a cylindrical porous block is installed and brazed inside to enhance the heat transfer rate. The structure of the porous medium was formed using a number of RR made of copper and coated with a gold alloy and brazed together with a porosity of 78.8%, the same material used in previous works [29,35]. As far as the thermal conductivity of porous material is concerned, it is believed that the brazing process could alter the thermal conductivity, leading to an unknown effective conductivity of the porous matrix. Although the RR cavity cooling system is patented by THALES, the precise dimension of the rings cannot be disclosed. As this study focuses on the one-side heating of the tubular absorbers, the RR porous medium was placed in the location where the peak of Gaussian-shaped flux forms to maximize the thermal energy exploitation and the rate of pressure drop growth. As a result, in addition to the smooth tube, two modified tubes were fabricated at THALES with RR porous inserts with a nominal length of 40 mm and 20 mm, to assess the effects of different porous lengths on the thermo-hydraulic behavior of the solar collector (Fig. 1b). In order to increase the thermal efficiency of the absorber, tubes were later coated with PYROMARK 2500 in black color, which improves the absorptivity up to 0.955 and has good durability in high-temperature applications [36]. Table 1 provides the main features of the sample

Table 1
Details of the tube absorbers used in this study.

Tube label	Porous length (L) (mm)	Coating	Tube length (H) (mm)	Diameter (D) (mm)	Wall thickness (mm)
uSP	None (smooth)	None	235 mm	25.4	2.2
SP	None (smooth)	PYROMARK 2500	235 mm	25.4	2.2
20RR	20 mm	PYROMARK 2500	235 mm	25.4	2.2
40RR	40 mm	PYROMARK 2500	235 mm	25.4	2.2

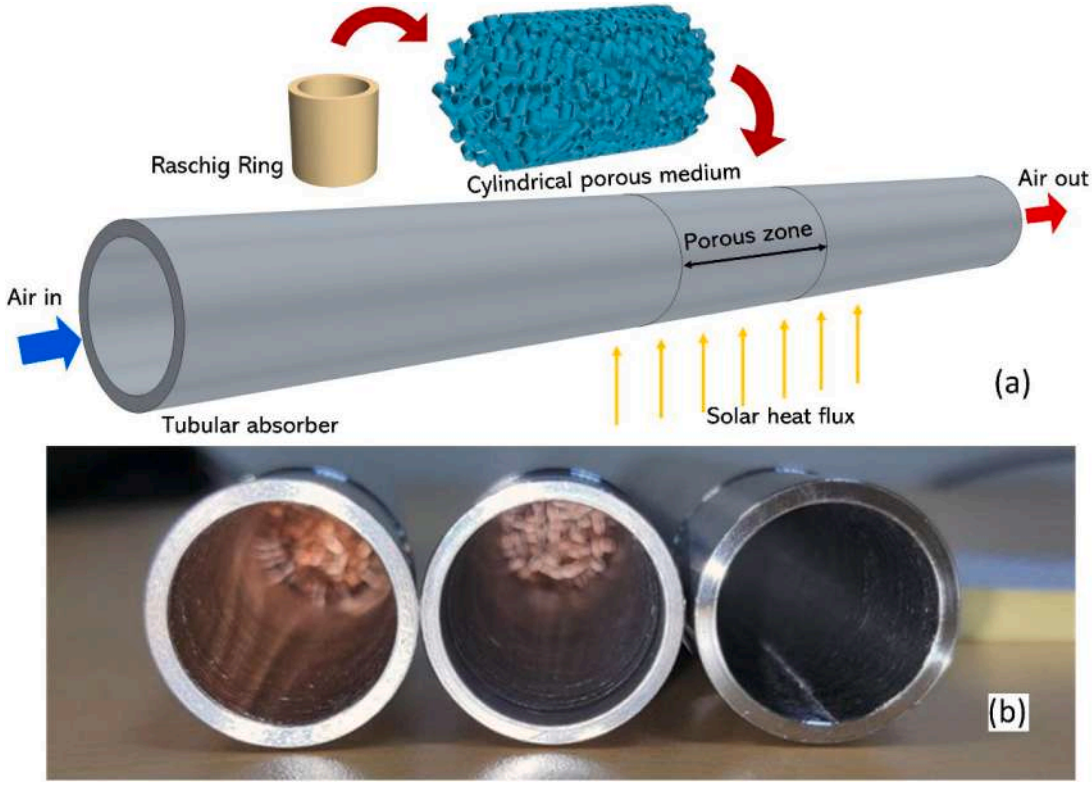

Fig. 1. The enhanced air tubular receiver; (a) schematic view of the porous insert, (b) picture of the smooth tube, and the two modified tubes with RR porous inserts (from right to left).

absorbers manufactured and tested in this study.

2.2. Solar furnace

The 0.08 MWth High-Flux Solar Furnace (SF60) at the Plataforma Solar de Almeria (PSA), Spain, was selected as the host of the experimental test campaign, in the frame of the SFERA-III Transnational Access Activities. As shown in Fig. 2, the main components of the solar furnace are a 130 m^2 heliostat as the primary reflector, a shutter opening to regulate the concentrated flux, a 108 m^2 surface reflection parabolic dish concentrator as the secondary reflector, and the receiver which is the tubular absorber in this test. Therefore, during the operation, the coming solar radiation to the heliostat, equipped with a two-axial tracking system, is reflected directly toward the shutter, providing the desired solar intensity through its adjustable windows. As the solar rays pass through the shutter, the parabolic dish concentrates them in the focal point, which is located on a test bed. As seen in Fig. 2d, the solar absorber is mounted in the test bed, facing the heat flux from one side, while a protective shield covers the redundant solar flux on its side to protect the test facility from high exposures. The table moves in three directions (East-West, North-South, up and down), placing the test samples in the focus with great precision. The nominal total power of the solar furnace is 80 kW with a peak irradiance of 6.7 MW/m^2 at the center when the shutter is 100% open, and the Direct Normal Irradiance (DNI) is 1000 W/m^2.

2.3. Experimental procedure

The experimental test campaign was carried out in June 2022 to evaluate the performance of the modified absorber and check the applicability of the proposed system. Technical assessments were done for four different absorber samples, including an uncoated smooth pipe (uSP), a coated smooth pipe (SP), a pipe with a 20 mm RR insert (20RR), and a pipe with a 40 mm RR insert (40RR), studying the hydraulic and thermal behaviors. The effects of the operating parameters, such as the airflow rate and solar heat flux were examined at three levels of each parameter on the thermo-hydraulic performance, with a total of 9 tests per sample. In addition to the thermal tests, a number of hydraulic tests were carried out under no-heating conditions, to purely measure the values of pressure drops in a range of airflow rates. As mentioned earlier, a comparative study was made on the SP to investigate the influence of the PYROMARK 2500 coating on the sample and find the increments of the efficiency enhancement. Therefore, in the first stage, experiments with the same operating conditions were applied on the SP one time before the coating (uSP) and one time after the coating (SP) to provide a fair comparison. In the second stage three coated samples were compared, using similar operating conditions. Full experiments were first conducted for each sample before installing the next one. Table 2 represents the details of experimental conditions on each test day.

In the process of heat flux measurement, from one side, it was known that the flux distribution follows a Gaussian shape [37], thus the peak heat flux was set as an identification for the flux report. On the other side, based on the operation principle of the solar collector, flux measurements must be done in series to the absorber heating. For this purpose, a white Lambertian target was installed beside the solar absorber, which was placed into the focal point by the table movement at the time of flux measurements. As the consequence, the solar peak flux was measured twice for each test; one time at the beginning of the test, when the desired flux was achieved through the shutter setting and one time after a complete irradiation period when all the temperatures of the samples reached a quasi-steady state condition. It is noteworthy to mention that, according to the working principle of the solar furnace, reaching a quite steady condition for sample temperatures is undoable [29], as a very small change in DNI results in a significant alteration in solar flux which varies the sample temperatures.

2.4. Test rig and measuring tools

In order to analyze the thermo-hydraulic behavior of the solar absorbers, an open-loop hydraulic circuit (primary loop) was provided to supply the pressurized air with various flow rates. As shown In Fig. 3, a 7.5 kW compressor with an inlet pressure of 10 bar injects the ambient air into the system with the aid of a flow regulator valve, setting various flow rates to cool the solar absorber. When the test bed is placed into the focal position, the concentrated solar energy is focused on the receiver's frontal side, heating the fluid with continuous air circulation. At the end of the primary loop, the heated air is cooled down by a cooling unit, using the water pumped by the pump from the secondary circuit, and consequently is exhausted. Cooling piping was also available for the Lambertian target, which used the pumped water from the secondary loop.

The thermal and hydraulic tests were achieved using a number of sensors discussed in the following;

- A F-203AV mass flowmeter with an accuracy of 2%, which is manufactured by Bronkhorst for gas fluids was located downstream after the cooling unit to measure the airflow rates during the experimental tests. The readout was in NL/min.
- A Pyrheliometer (model: CH-1) manufactured by Kipp & Zonen was used outdoors, next to the heliostat to record the intensity of solar beam radiations or DNI (W/m^2) with an accuracy of 3%.
- The employment of a PD-type differential pressure sensor manufactured by Aplisens with a static pressure limit of 40 bar led to the measurement of the pressure difference across the test section. Readings were performed with an accuracy of $\pm$ 2.40% + 5 mbar for the measurements of total pressure drop across the testing section, including some joint and concoction losses due to the connections and piping. The values of the net pressure drop were computed, subtracting the contribution of the minor losses evaluated as reported in [15].
- Using a pressure transmitter (Model S-10) manufactured by WIKA, with a measurement full range of 1000 bar and a nonlinearity of

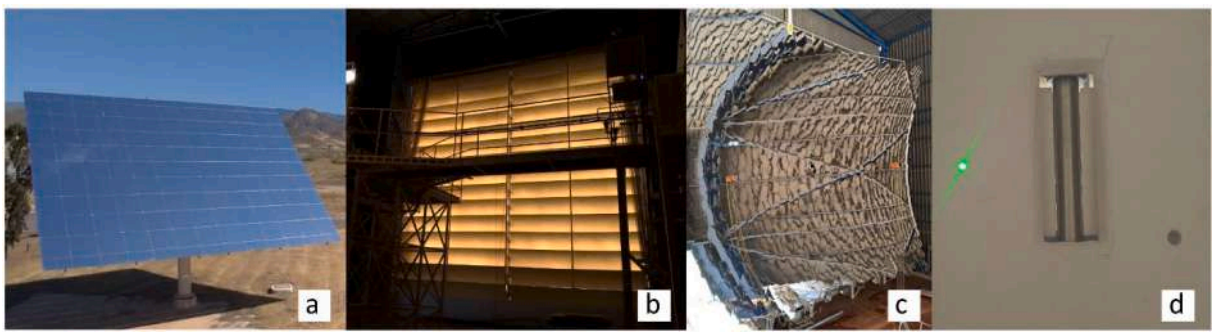

Fig. 2. The main components of the solar furnace (SF60) at the PSA, including: (a) heliostat, (b) shutter, (c) parabolic collector, (d) receiver and the shield.

Table 2
Details of the experimental tests. The test ID is given for each test by the concatenation of the targeted heat flux value with the flow rate value.

Sample	Date (DD/MM/YY)	Test ID	Peak heat flux (kW/m^2) Before	After	Nominal Airflow rate (NL/min)	Ambient temperature (^{o}C)	Shutter aperture (%)	DNI (W/m^2)	Inlet pressure (bar)
uSP	09/06/22	5030	51.1	48.5	30	31.0	2.7	875.9	9.6
		5040	48.6	52.1	40	32.5	2.7	900.3	9.7
		5050	47.7	50.3	50	33.5	2.7	892.0	9.8
		10030	107.5	110.4	30	28.0	3.9	853.7	9.4
		10040	100.9	105.7	40	26.4	4	785.7	9.5
	10/06/22	10050	108.4	103.9	50	34.7	3.6	873.0	9.5
		20030	205.0	195.7	30	34.5	5.2	972.1	9.5
		20040	206.2	190.2	40	33.6	5.3	964.2	9.5
		20050	201.1	203.3	50	32.2	5	955.3	9.2
SP	22/06/22	5030	48.3	50.7	30	28.6	2.7	981.1	9.9
		5040	50.3	47.1	40	29.8	2.7	995.3	9.2
		5050	48.1	48.2	50	30.4	2.7	999.2	9.6
		10030	96.5	106.0	30	31.1	3.8	1012.9	9.8
		10040	99.9	96.9	40	32.0	3.6	1032.0	9.8
		10050	99.4	102.8	50	33.2	3.6	1018.6	9.6
	23/06/22	20030	197.8	196.0	30	28.5	5.7	951.5	9.3
		20040	198.6	199.8	40	34.5	5.5	997.4	10.0
		20050	201.8	203.0	50	27.4	5.8	934.7	9.2
20RR	16/06/22	5030	48.9	48.6	30	30.9	4.1	419.5	9.3
		5040	48.0	52.4	40	33.9	3.4	557.9	10.8
		5050	51.5	50.4	50	33.4	3.5	529.6	10.2
		10030	95.6	98.8	30	34.5	4.9	596.0	10.0
		10040	100.3	102.4	40	35.3	4.3	627.9	9.8
		10050	102.4	103.4	50	36.0	4.3	652.1	10.2
		20030	198.1	199.3	30	36.5	6.8	673.3	9.7
		20040	198.3	189.9	40	38.7	6.7	708.2	9.5
		20050	201.8	199.3	50	39.3	6.6	706.8	9.7
40RR	17/06/22	5030	50.2	49.6	30	32.5	3.3	580.2	10.3
		5040	48.5	44.9	40	34.5	3	643.7	9.37
		5050	48.8	45.2	50	35.5	3.1	685.1	9.6
		10030	99.8	103.7	30	36.4	4.4	705.8	9.7
		10040	103.1	105.0	40	37.0	4.2	742.6	9.6
		10050	100.2	91.8	50	37.6	4	756.7	9.5
		20030	204.3	193.8	30	38.8	6.5	746.3	9.7
		20040	199.0	201.5	40	39.5	6.3	753.3	10.2
		20050	201.0	196.0	50	40.1	6.2	745.3	10.0

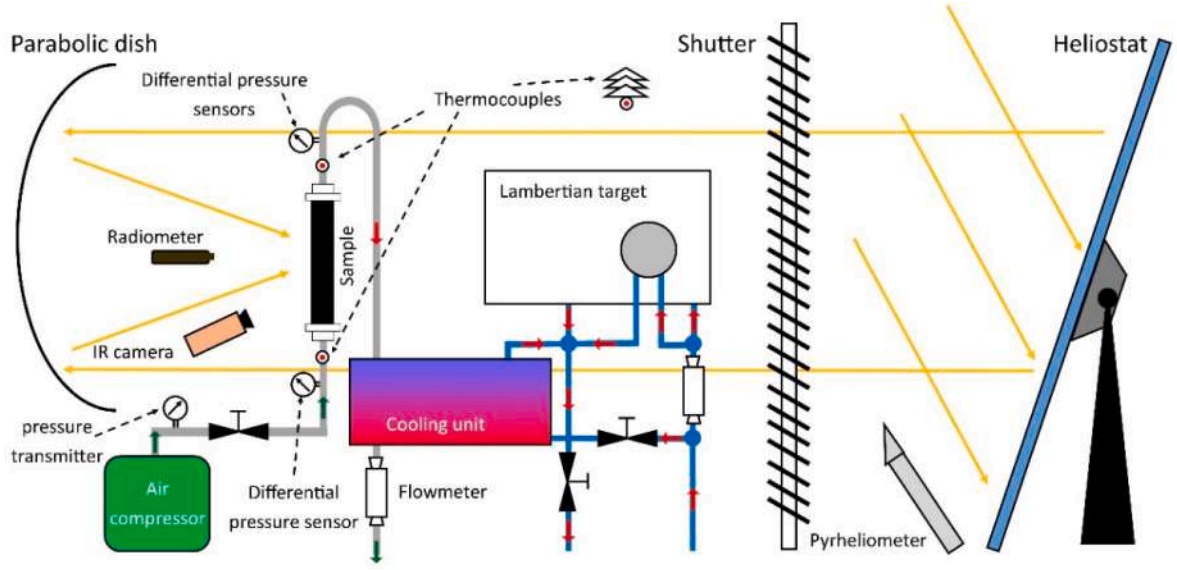

Fig. 3. Sketch of the experimental test setup and location of the measuring tools.

0.2%, the operating pressure of the system was evaluated continuously.

- A water-cooled ASYMPTOTIC circular foil calorimeter was also utilized for high heat flux measurements with an accuracy of 3%. The position of the radiometer was in the front of the focus point and when the table was moved to the Lambertian target, it could see the flux and measure the amplitude of the solar peak flux.
- The temperature sensors were selected among the K-type, with a Class Tolerance I (±1.5 °C in the range of −40 °C to 375 °C and 0.004×|T|, where T is the measured temperature in Celsius (^{o}C), in

the range of 375–1000 °C). One thermocouple was set in the test facility for ambient temperature measurement, one was used for the air inlet and one was used for the air outlet temperatures as shown in Fig. 3. A different number of thermocouples were mounted on the backside of the samples (3 for SP, 7 for 20RR and 40RR) in order to not being affected by the direct solar irradiance, and also give a full understanding on the temperature profile of tube wall. For this purpose, several small grooves with less than 1 mm depth were made on the tube wall based on the different distances from the tube endings. Then the sensor connectors were welded to the tube, letting the insertion of the thermocouple in a way that its tip was in full contact with the wall. Fig. 4a and 4b show the location of thermocouples for each sample. Please note that the arrangements of the thermocouples in both 20RR and 40RR samples are the same as the schematic shows in Fig. 4b, thus only one thermocouple (TC02) is located in the porous zone of the 20RR sample.

- In addition to the thermocouples, an infrared camera from Optris with an uncertainty of 2% was employed for thermal imaging from the frontal side of the samples, evaluating the hotspots on the heated surface. Fig. 4c illustrates the location of the camera with respect to the test table in the way that the solar flux is not affected by the camera position. For the operation, every day, the camera was turned on one hour before the testing period to reach its stable condition. Then, calibrations took place based on the instructions indicated by the manufacturer, setting the desired emissivity (ε) and temperature range according to the testing materials. For this purpose, and in order to find the correct emissivity for the coating used in this study, several tests were performed before the real tests, locating the thermal camera on the rear side of the sample to read the temperatures also recorded by the thermocouples (Fig. 5). In this regard, a wide range of emissivity was used to calibrate the IR camera based on the thermocouples and it was found that $0.85 < \varepsilon < 0.90$ suits the operating range of this study, which is aligned with the results reported in [38].

2.5. Data analysis

This section provides the details of experimental energy and exergy parameters to determine the thermal performance of the samples.

From the energetic point of view, the total energy rate received from the solar radiation ($E_{(s-Hel)}$) is equal to the amount collected by the heliostat and can be expressed as Eq. 1.

$$E_{(s-Hel)} = A_{he} G \tag{1}$$

where A_{he} is the area of the heliostat, and G is the direct normal irradiance from the sun to the heliostat. In this study, the solar peak flux is one of the investigated parameters, which was regulated during the experiments by the shutter opening percentage. Therefore, the solar power that passes through the shutter and reaches the parabolic dish (E_{S-Dish}) is given as Eq. 2.

$$E_{(S-Dish)} = \omega E_{s-Hel} \tag{2}$$

In which ω is the aperture fraction (%) of the shutter. Furthermore, the solar energy rate concentrated in the focus is a function of the optical performance (η_o) of the parabolic dish and can be expressed as Eq. 3, where η_o is the optical efficiency of the parabolic dish.

$$E_{(S-focus)} = \eta_o E_{s-Dish} = \eta_o \omega A_{he} G \tag{3}$$

Direct determination of the amount of solar flux that reaches the sample in solar furnaces has been well-documented in the literature [39,40]. Based on the theories, the spatial distribution of the solar flux is rotationally symmetric with the peak in the center, however, in the real tests, there are some factors such as the concentrator shape and shutter blades that can influence its distribution [41]. Therefore, the

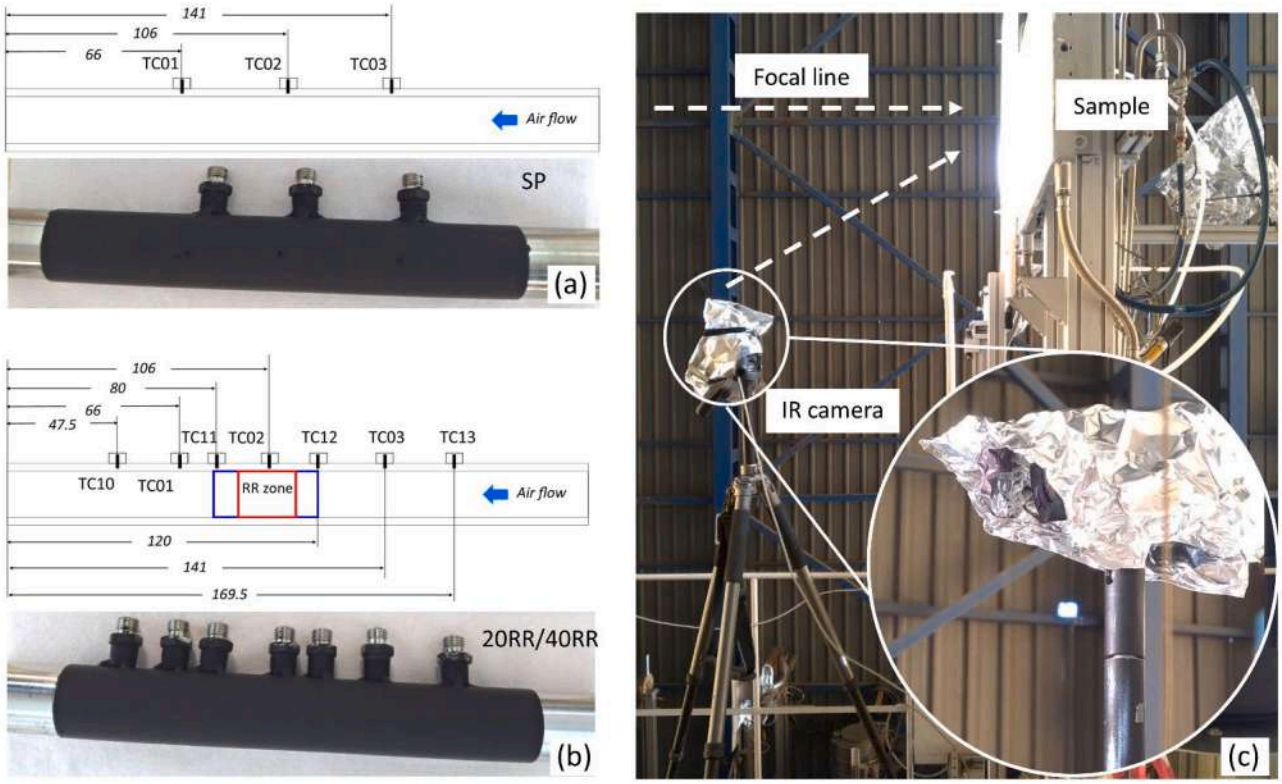

Fig. 4. Details of the temperature sensors used during the experiments; (a) thermocouples mounted on uSP and SP samples (dimensions are in mm), (b) thermocouples mounted on 20RR and 40RR samples, where the red and blue regions reflect the RR zone in the 20RR and 40RR designs, respectively (dimensions are in mm), (c) the lR camera employed for temperature recording from the heated part of the samples. (For interpretation of the references to color in this figure legend, the reader is referred to the web version of this article.)

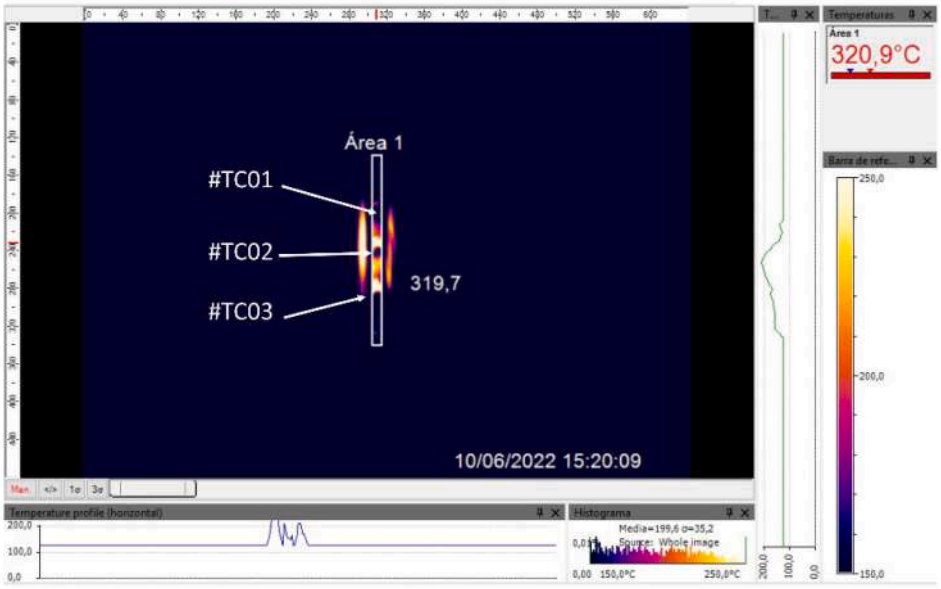

Fig. 5. Calibration of IR camera, reading the temperatures of the thermocouples from the backside of the SP absorber.

concentrated solar flux imposed on the focus ($E_{(S-focus)}$) was considered using Eq.4. as a function of the power on the plane perpendicular to the solar irradiance [37].

$$E_{(S-focus)} = \iint \varphi_{peak} \times e^{-0.5\left[\left(\frac{x}{\sigma_x}\right)^2+\left(\frac{y}{\sigma_y}\right)^2\right]} dxdy \tag{4}$$

where φ_{peak} is the concentrated solar radiation (W/m^2) measured at the focus on the Lambertian target, x and y are the length in two coordinate axes, one in the azimuthal and the other in longitudinal directions, while σ_x and σ_y are the standard deviations, corresponding to x and y directions, equal to 0.053 and 0.050 m [42].

As the total power in the focus can be represented as a circle with a diameter of 22 cm, using Eq. 4 for the range of -11 cm $< x <$ 11 cm and -11 cm $< y <$ 11 cm, then combing with Eq. 3, the optical efficiency of the parabolic dish can be obtained as Eq. 5.

$$\eta_o = \frac{\iint \varphi_{peak} \times e^{-0.5\left[\left(\frac{x}{\sigma_x}\right)^2+\left(\frac{y}{\sigma_y}\right)^2\right]} dxdy}{A_{he}\omega G} \tag{5}$$

For this purpose, a series of tests were performed at the PSA and prior to the main investigations of this study, varying the shutter opening and measuring the total power received at the focus. Results are depicted in Fig. 6, indicating the best-fit function with an R^2 of 0.99 to be used as the optical efficiency of the parabolic dish.

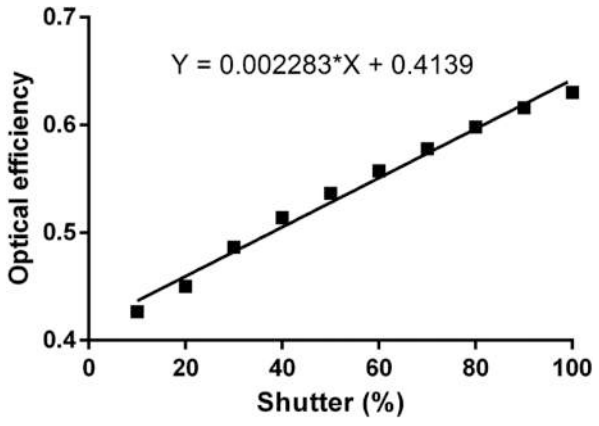

Fig. 6. Optical efficiency of the parabolic dish as a function of the shutter opening.

In order to evaluate the amount of power received on the circumference of the tubular receiver, Eq. 6 is introduced to consider θ, the power incident angle, while the integration bonds are modified as $-\frac{D}{2} < x < +\frac{D}{2}$ and $-\frac{L}{2} < y < +\frac{L}{2}$.

$$E_{(S-Cfocus)} = \iint \varphi_{peak} \times e^{-0.5\left[\left(\frac{x}{\sigma_x}\right)^2+\left(\frac{y}{\sigma_y}\right)^2\right]} dxdycos\theta \tag{6}$$

The absorbed solar energy is converted into useful heat and is then transferred by the HTF, increasing the temperature of the running air. Therefore, the useful energy rate can be determined as Eq. 7.

$$E_u = mc_p(T_o - T_i) \tag{7}$$

where m denotes the air mass flow rate, c_p is the specific heat of air at the mean temperature ($T_m = \frac{T_i+T_o}{2}$), while T_i and T_o are respectively the inlet and outlet temperature of the air.

While a fraction of the absorbed solar energy rate is converted into useful heat, the rest is dissipated to the environment as heat loss (E_L) in terms of radiation and convection. Thus, Eq. 8 can be used to show the values of the total heat loss.

$$E_{(S-Cfocus)} - E_u = E_L = U_L A_r(T_m - T_{amb}) \tag{8}$$

where U_L is the total heat loss coefficient, A_r is the receiver area, and T_{amb} represents the ambient temperature.

The energetic efficiency of the absorber can be defined as the ratio between the useful power (E_u) and the total concentrated power reaching the absorber ($E_{(S-Cfocus)}$), shown in Eq. 9.

$$\eta_{en} = \frac{E_u}{E_{(S-Cfocus)}} \tag{9}$$

If an exergy analysis is performed rather than an energetic one, the useful exergy rate given to the running air can be written as Eq. 10.

$$Ex_u = E_u - mc_pT_{amb}\ln\left(\frac{T_o}{T_i}\right) = mc_p\left[(T_o - T_i) - T_{amb}\ln\left(\frac{T_o}{T_i}\right)\right] \tag{10}$$

And according to [43,44] the exergy rate of the solar radiation concentrated by the parabolic dish ($Ex_{(S-Cfocus)}$) can be expressed as Eq. 11.

$$Ex_{(S-Cfocus)} = E_{(S-Cfocus)}\left[1+\frac{1}{3}\left(\frac{T_{amb}}{T_s}\right)^4-\frac{4T_{amb}}{3T_s}\right] \tag{11}$$

where T_s denotes the surface temperature of the sun and is usually predicated as 5762 K.

As a result, the exergy efficiency which provides the amount of total concentrated radiation exergy that has been used by the receiver for the useful exergy would be determined using Eq. 12.

$$\eta_{ex} = \frac{Ex_u}{Ex_{(S-Cfocus)}} = \frac{mc_p\left[(T_o-T_i)-T_{amb}\ln\left(\frac{T_o}{T_i}\right)\right]}{\iint \varphi_{peak}\times e^{-0.5\left[\left(\frac{x}{\sigma_x}\right)^2+\left(\frac{y}{\sigma_y}\right)^2\right]}dxdycos\theta\left[1+\frac{1}{3}\left(\frac{T_{amb}}{T_s}\right)^4-\frac{4T_{amb}}{3T_s}\right]} \tag{12}$$

$$W_{Re} = \left[\left(\frac{\partial R}{\partial x_1}w_1\right)^2+\left(\frac{\partial R}{\partial x_2}w_2\right)^2+\cdots+\left(\frac{\partial R}{\partial x_n}w_n\right)^2\right]^{\frac{1}{2}} \tag{15}$$

In which W_{Re} denotes the resulting total uncertainty and w_1, w_2, …, w_n represent the uncertainties of the independent variables. In this study, the uncertainty variables consist of the fluid mass flow rate, solar concentrated flux, ambient, inlet, and outlet temperatures, where the relative equations for uncertainties in energy and exergy efficiencies are given in Eqs. (16) and (17), and the details of the experimental errors are provided in Table 3.

$$W_{\eta_{en}} = \left[\left(\frac{\partial \eta_{en}}{\partial E_{(s-Cfocus)}}w_{E_{(s-Cfocus)}}\right)^2+\left(\frac{\partial \eta_{en}}{\partial m}w_m\right)^2+\left(\frac{\partial \eta_{en}}{\partial T_i}w_{T_i}\right)^2+\left(\frac{\partial \eta_{en}}{\partial T_o}w_{T_o}\right)^2\right]^{\frac{1}{2}} \tag{16}$$

$$W_{\eta_{ex}} = \left[\left(\frac{\partial \eta_{ex}}{\partial E_{(s-Cfocus)}}w_{E_{(s-Cfocus)}}\right)^2+\left(\frac{\partial \eta_{en}}{\partial m}w_m\right)^2+\left(\frac{\partial \eta_{en}}{\partial T_i}w_{T_i}\right)^2+\left(\frac{\partial \eta_{en}}{\partial T_o}w_{T_o}\right)^2+\left(\frac{\partial \eta_{en}}{\partial T_{amb}}w_{T_{amb}}\right)^2\right]^{\frac{1}{2}} \tag{17}$$

In order to provide a fair comparison between the result of this study with those conducted in a similar context, a unique criterion as Energy Efficiency Enhancement Factor (*EEEF*) is defined as Eq. 13. This factor reveals the highest energy efficiency achieved by the enhanced method (η_{en}) compared to those obtained by the basic design (η_{std}) considered in the evaluation process.

$$EEEF = \frac{\eta_{en}-\eta_{std}}{\eta_{std}} \tag{13}$$

2.6. Analysis of the experimental uncertainty

The source of the experimental errors includes the uncertainties coming from the measuring tools, which can be converted into the independent variables and their relation with the main dependent factors. According to Holman [45], the following expressions can be used for the evaluation of the uncertainties in dependent functions.

$$R = R(x_1, x_2, x_3, \cdots, x_n) \tag{14}$$

Supposing that the result R is a given function of the independent variables x_1, x_2, x_3, …, x_n, therefore.

Table 3
Error sources of the experimental results and their relative uncertainties.

Variable	Uncertainty	Value
Solar concentrated flux	$w_{E_{(s-Cfocus)}}$	±3%
Airflow rate	w_m	±2%
Air inlet temperature	w_{T_i}	± 1.5 K
Air outlet temperature	w_{T_o}	± 1.5 K
Thermocouple temperature	$w_{T_{TC}}$	± 1.5 K
Ambient temperature	$w_{T_{amb}}$	± 1.5 K
Pressure drop	$w_{\Delta p}$	±2.40% + 5 mbar
Hotspot temperature	$w_{T_{hot}}$	2%
Average useful heat	w_{E_u}	8.3%
Average heat loss	w_{E_L}	16%
Average energy efficiency	$w_{\eta_{en}}$	12.6%
Average exergy efficiency	$w_{\eta_{ex}}$	12.7%

3. Results and discussion

3.1. Hydraulic characteristics

As was mentioned earlier, pure hydraulic tests were carried out under no heating conditions to check the pressure drop in each absorber tube. Fig. 7 represents the results of the hydraulic tests for the three samples, showing that, with an increase in flow rate, the total pressure drop rises in all the tests. Here the total pressure drops are the measured value across the testing section, which includes also the major and minor losses through the piping and connection at both ends of the samples. As expected, the 40RR sample results in the highest pumping penalty, followed by the 20 RR and SP. Comparing the values, it was obtained that with the highest flow rate (800 L/min) the RR insert could increase the pressure drop by ~ 300% and ~ 400% with a length of 20 and 40 mm, respectively.

According to the literature [46], when a gaseous fluid passes through packed beds at high velocity, there is a non-linearity between the fluid flow rate and the driving pressure drop, and this increases the inertia

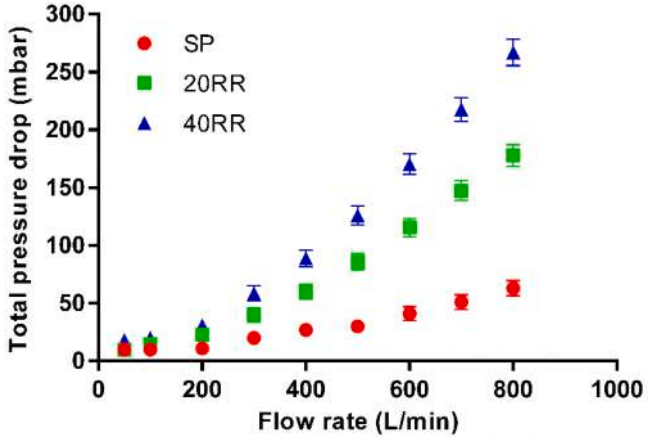

Fig. 7. Fluid pressure drop of different sample models and various flow rates.

effects. Therefore, under turbulence conditions, Darcy law could not define the velocity field of fluid flow in a porous medium and Darcy–Dupuit–Forchheimer model, with also a quadratic dependence on the velocity, is introduced as Eq. 18.

$$\frac{\partial p}{\partial x_i} = -\frac{\mu}{\alpha} v_s + 0.5\rho C|v|v_S \tag{18}$$

In Eq. 18, p, x , and v_s are respectively the fluid pressure, the length of the porous material, and inlet superficial velocity. Moreover, the two variables $1/\alpha$ and C are the viscous and inertial resistance coefficients in the direction of the airflow, respectively representing linear and nonlinear pressure behavior (drop) along the porous material [47]. To evaluate the inertia and viscous resistance, the pressure drop characteristics of the porous medium fitted with a parabolic curve were used, which can be presented in the form reported in Eq. 19.

$$\frac{\partial p}{\partial x_i} = a v_s^2 + b v_s \tag{19}$$

In the next step, if Eq. 18 and 19 are compared, the viscous and inertia coefficients are determined as Eq. 20 and 21.

$$\frac{1}{\alpha} = \frac{b}{\mu} \tag{20}$$

$$C = \frac{2a}{\rho} \tag{21}$$

Fig. 8 illustrates the plots of the ratio of pressure drop over porous length ($\Delta P/L$) as a function of air velocity. In this evaluation, L is the porous length, taken as 20 and 40 mm in 20RR and 40RR samples, respectively, and ΔP corresponds to the pressure difference over the porous insert and excludes the pressure loss due to the pipe and connectors. Therefore, in this plot, ΔP has been calculated by the subtraction of the pressure loss in the SP from those of the modified tubes (20RR and 40RR). It is observed that both plots are following the same pattern with close values. The residual difference is due to the localized pressure drop at the inlet/outlet of the RR block, which has a bigger weight on the pressure drop in the pipe with the shortest RR length. Fig. 8 also demonstrates that the inertia and viscous resistances remain constant for a porous medium with a given porosity and are regardless of the porous length. Therefore, the best fitting curve with an $R^2 > 0.99$ for the average values in addition to the implementation of Eqs. 20 and 21 result in a correlation which gives $1/\alpha$ and C as $7.13 \times 10^8 \pm 4.85 \times 10^8$ m^{-2} and $5.37 \times 10^3 \pm 5.6 \times 10^2$ m^{-1}, respectively. Comparing these results with those reported for RR porous materials with simulations by [48] as 6.00×10^8 m^{-2} and 8.07×10^3, it can be concluded that the values of viscous resistances are within an acceptable tolerance. In terms of inertia resistances, the increments refer to the discard of the effects of brazing material in the simulations, as well as the large experimental and numerical errors.

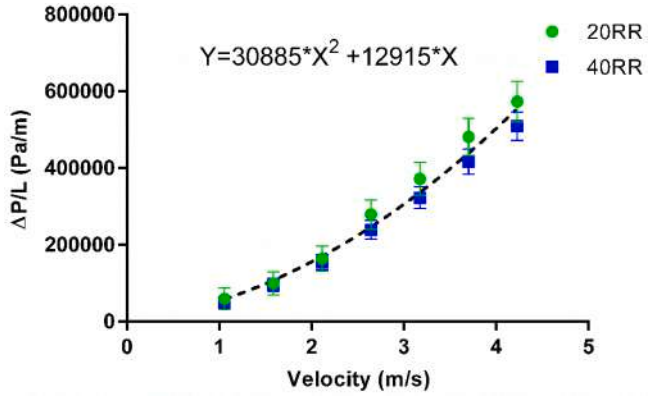

Fig. 8. Variation of pressure drop over the porous thickness as a function of superficial air velocity. L is the porous length and ΔP is the pressure difference over the porous insert.

3.2. Thermal performance

3.2.1. Temperature profile

In this section, the temperature variation of the tube wall, as well as the temperature difference of the HTF, have been compared among all four different samples. In this regard, Fig. 9 represents the temperature rise of the smooth sample for a typical test period, working under 200 kW/m^2 peak flux and 50 L/min airflow rate. As shown, the temperatures were recorded based on the temperature growth from the initial values, starting from zero for all temperature sensors. Exposing the sample to concentrated solar radiation, the transient phase starts and temperatures of the tube wall increase as well as the outlet temperature, while the inlet temperature remains constant. This temperature rise continues until reaching a quasi-steady state after 900 s, where tube wall temperature keeps a constant level with some slight changes and the outlet temperature becomes smooth. Remaining at this stage for nearly 1000 s, temperature readings were performed and consequently, solar exposure was stopped, shifting the test rig to focus on the Lambertian target. It is also important to mention that during the test, the DNI level was not changing dramatically in time, helping in reaching the quasi-steady state faster. Comparing the temperature of the thermocouples, it is concluded that TC02, which is located in the middle of the tube, has the maximum temperature rise with a value of 280 °C, proving that the peak of the Gaussian shape flux was within TC03 and TC01. Note that TC03 and TC01 are nearly close, but a slight rise in TC03 is seen between 1100 s and 1900 s, which is possibly due to the wind effects on the heliostat and temporary changes in the position of the concentrated flux on the tube wall. Analyzing the cooling process (unloading phase), TC03 has the highest cooling rate, followed by TC02 and TC01, respectively. This behavior is based on the location of the sensors, where the one closer to the inlet receives fresh coolant with negligible heat to remove upstream, in view of the Gaussian shape of the heating.

Fig. 10 shows a testing procedure for a modified pipe (40RR5050), in which four more thermocouples have been utilized with respect to the SP. The transition period lasts nearly 800 s, similar to those of SP in Fig. 9. Continuing the test, the quasi-steady state is reached and lasts until 1200 s, where most of the measured temperatures are stable. Eventually, the unloading phase started where temperatures declined at different rates respecting the location of the sensors. Comparing the temperatures of different sensors, it is apparent that TC02, which is located right above the peak flux, is the coolest point on the tube wall, due to the cooling effects induced by the 40 mm RR porous insert. This is also evident where TC02 shows the highest cooling rate on the tube wall during the unloading process, which reflects the effects of a higher wetted area and improved heat transfer between the air and the heated surface in the porous zone. The measurements at TC01 and TC03 show that in this test configuration, they are the two hottest points recorded, with respectively 48% and 50% higher temperature rise than TC02. This temperature distribution was also found through the simulations on a tube equipped with the porous medium under one-side heating [34]. Comparing the values measured with TC12 and TC11, the two thermocouples that are mounted at the beginning and ending of the RR porous zone, shows that TC11 has a 30% higher temperature rise than TC12. This could be due to a small misalignment of the focal point of the concentrator, which was unavoidable and a product of the of wind effects on the heliostat, since in principle a lower temperature rise downstream of the porous insert is expected in view of the air stream turbulence increase driven by the porous insert.

The temperature rise on the tube walls is depicted in Fig. 11 for the full experiments conducted on each sample. As expected, by increasing the airflow rate at each level of solar exposure, the tube wall temperatures decrease. However, there is an exception in sample uSP, where for the peak flux of 100 and 200 kW/m^2, increasing the airflow rate has

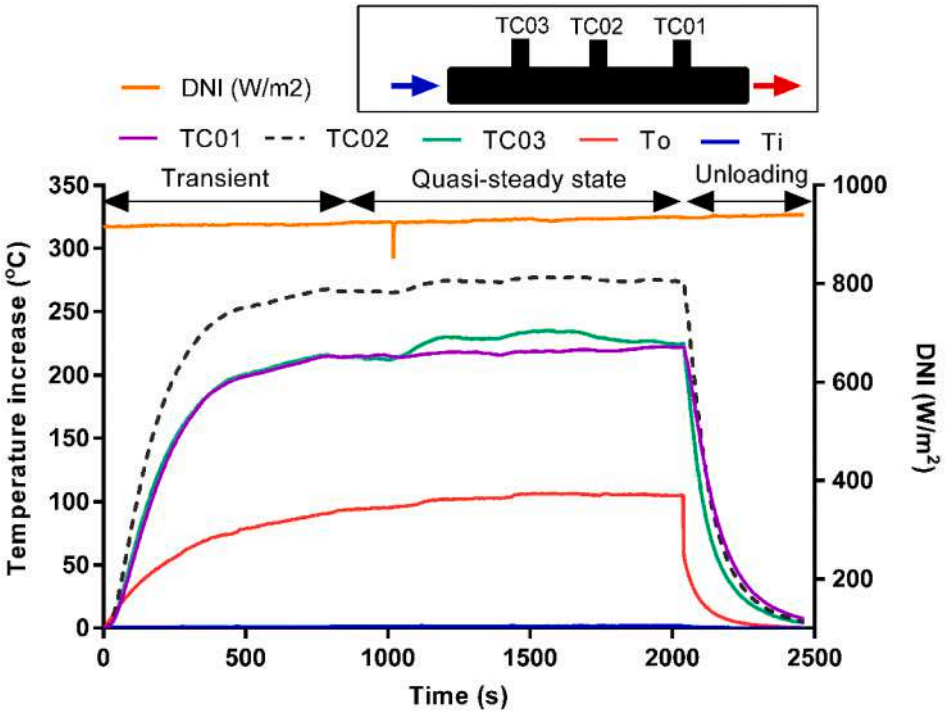

Fig. 9. DNI and receiver's temperature profiles during SP20050 test.

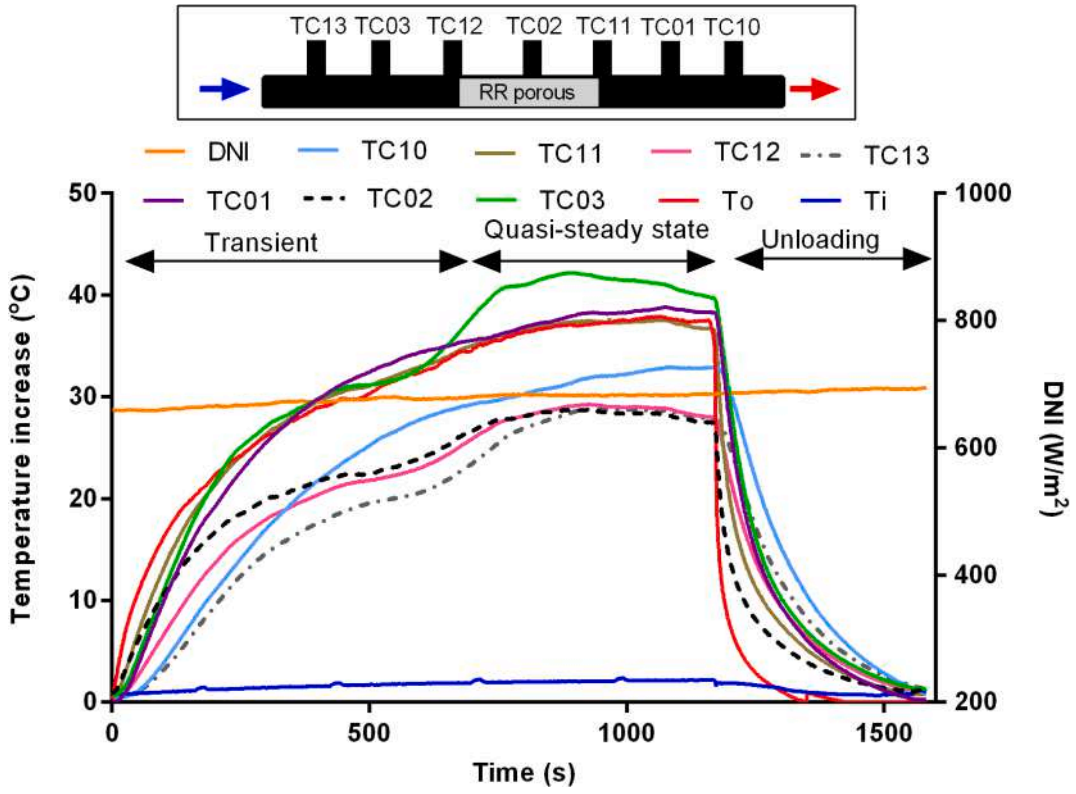

Fig. 10. DNI and receiver's temperature profiles during 40RR5050 test.

resulted in an increase in temperature rise on the tube walls. The reason for such behavior can be attributed to the oxidation that occurred at medium and high flux tests as shown in Fig. 12. This indicates that the concentrated heat flux can alter the wall surface properties by oxidizing it, providing changes in emissivity ε and absorptivity α_r that have affected the wall region. Since the tests were consecutive, and larger flow rates were tested later, the oxidation effect is more evident in tests at the higher flow rates, for which the cumulative effect of the oxidation has dominated and increased the tube wall temperature accordingly. Very similar effects were also seen in the work conducted by Cantone

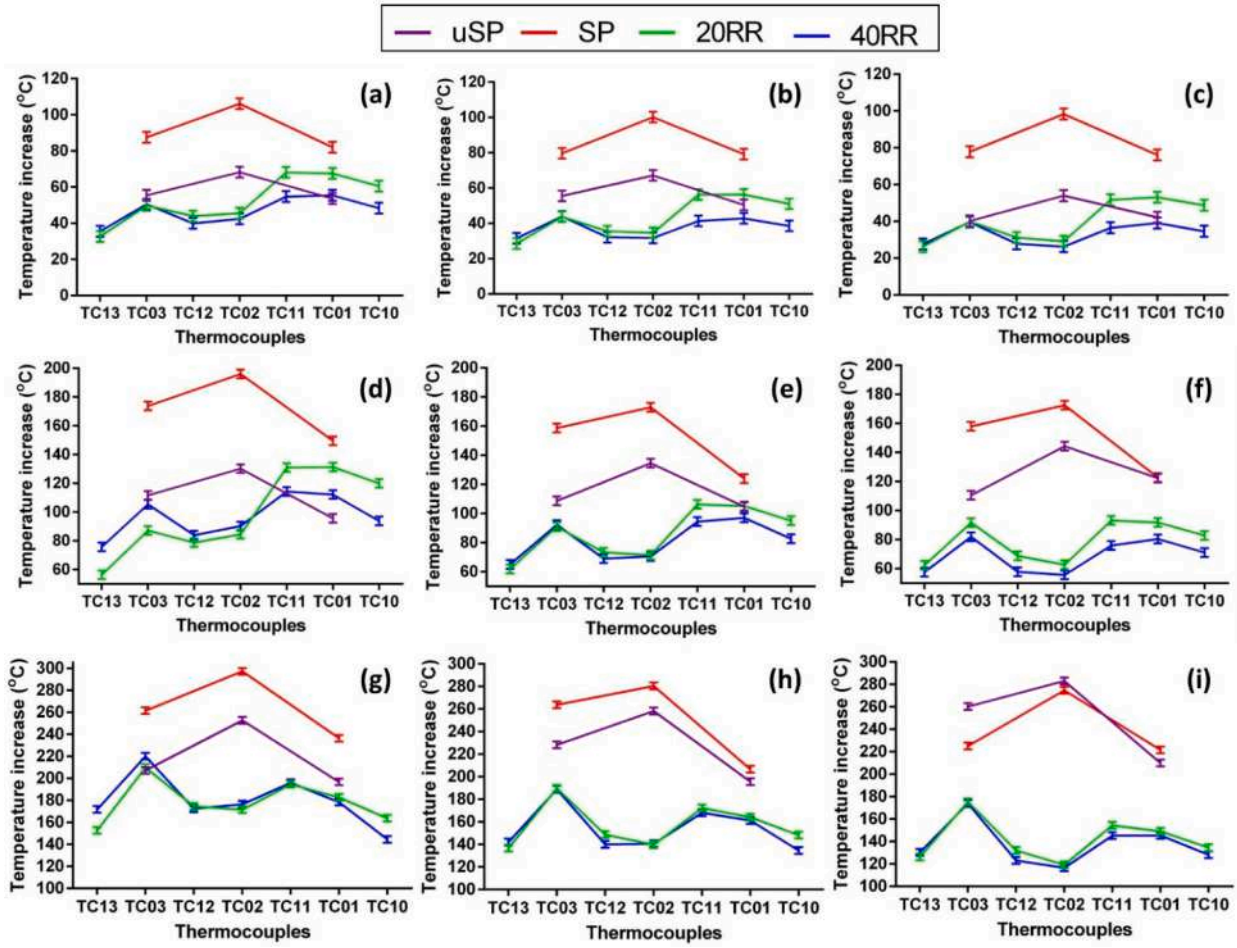

Fig. 11. Temperature increase on tube wall for different absorber designs, operating under (a) $\varphi_{peak} = 50$ kW/m^2 and $m = 30$ L/min, (b) $\varphi_{peak} = 50$ kW/m^2 and $m = 40$ L/min, (c) $\varphi_{peak} = 50$ kW/m^2 and $m = 50$ L/min, (d) $\varphi_{peak} = 100$ kW/m^2 and $m = 30$ L/min, (e) $\varphi_{peak} = 100$ kW/m^2 and $m = 40$ L/min, (f) $\varphi_{peak} = 100$ kW/m^2 and $m = 50$ L/min, (g) $\varphi_{peak} = 200$ kW/m^2 and $m = 30$ L/min, (h) $\varphi_{peak} = 200$ kW/m^2 and $m = 40$ L/min, (i) $\varphi_{peak} = 200$ kW/m^2 and $m = 50$ L/min.

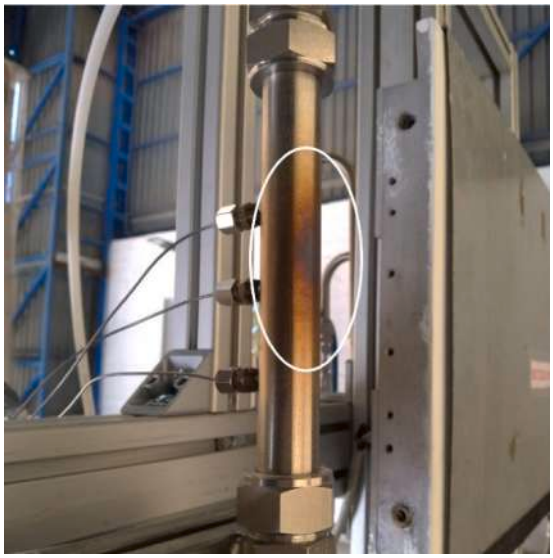

Fig. 12. Picture of the uSP sample with the oxidation appeared on the heated area and after the experimental tests.

et al. [15]. Moreover, the temperature difference between various airflow rates becomes more significant, increasing the solar flux, where the 200 kW/m^2 solar peak flux represents the maximum variations in each design. Comparing the uSP with SP, the rise in tube wall temperatures increases after the coating is applied, which shows although the heat transfer coefficient remains roughly the same inside the tube, the main effect of PYROMARK 2500 application is on the growth in solar absorption leading to larger heat transfer. In more detail, the lower peak flux levels render higher increments with coating, where the average tube wall temperature increase was 85.3% at a peak flux of 50 kW/m^2 and an airflow rate of 50 L/min. Note that, in the case of the painted tube, the highest flow rate provides, for the same heat flux, the lower temperature increase, as expected. Besides, increasing the airflow rate has decreased the temperature differences between uSP and SP.

The comparison of the wall temperatures between the smooth pipes and pipes equipped with RR inserts proves that the RR porous insert has tremendously cooled the absorber wall, resulting in lower temperature levels. Considering the temperature distribution along the pipes, the porous insert has changed the temperature increase profile, resulting in two peaks, one before and one after the porous zone. The behaviour is mostly depicted by TC03 and TC11, which was also seen in numerical simulations [34] and confirmed experimentally by the thermal images taken by the IR camera, as shown in Fig. 13.

More specifically, results show that the utilization of 20 and 40 mm RR reduces the tube wall temperature rise all along the pipe, where the maximum reduction (70%) takes place in the middle of the porous zone, for TC02 compared to the SP, with the 40RR sample operating

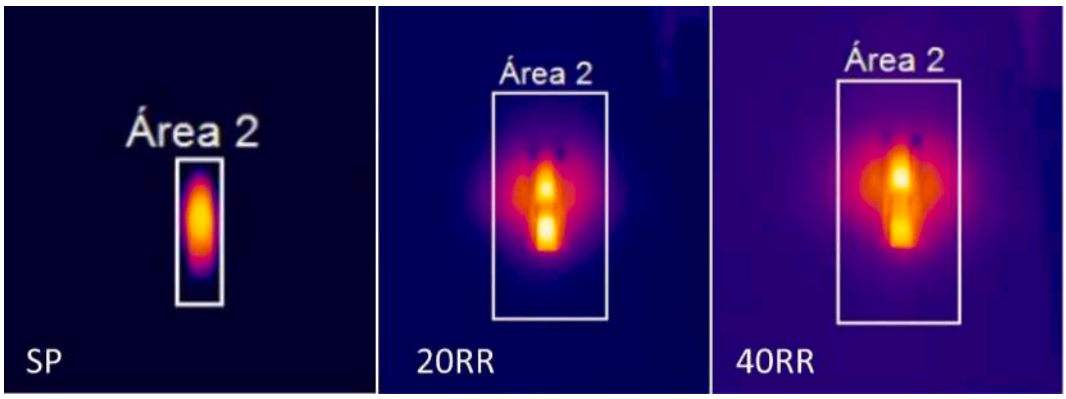

Fig. 13. Thermal images taken from three different absorbers operating under Peak flux = 100 kW/m^2 and m = 40 L/min.

under solar peak flux of 50 kW/m^2 and an airflow rate of 50 L/min. Also, it was observed that when the solar flux increases or airflow decreases the cooling enhancement is reduced. Comparing the two modified tubes, 40RR results in a relatively higher temperature rise reduction due to the longer porous medium integration, where the maximum deviation was obtained at a solar peak flux of 50 kW/m^2 and an airflow rate of 50 L/min with an average reduction of 14% on all temperature points. Note that the highest temperature rise reduction refers to TC10, followed by TC11 and TC01. This can be explained by the argument that, when the porous medium gets longer, it produces a considerable thermal mixing and results in higher thermal enhancement, providing lower temperature increase downstream, as already argued in [34] on the basis of a numerical study. Moreover, TC11 and TC12, the two thermocouples located in the extended porous zone compared to 20RR, also undergo significant improvements (respectively 14 and 6.5% further temperature rise reductions) in the 40RR sample, if compared to the 20RR sample, thanks to the elongation of the porous medium.

Note also that the higher the heat flux, the lower the difference between 20RR and 40RR appears. This demonstrates that, as the solar exposure becomes larger, temperature levels of the tube rise, diminishing the enhancing effects of the RR porous inserts up and downstream. However, the cooling effects observed at the porous zone, which is mostly due to the presence of the porous, remain less affected by changes in the solar flux.

The utilization of thermal cameras led to the peak temperature rise measurement on the front side of the tubes and the results are depicted in Fig. 14. As the IR measurements are based on the emissivity of the target surface, the coated absorbers including SP, 20RR and 40RR are

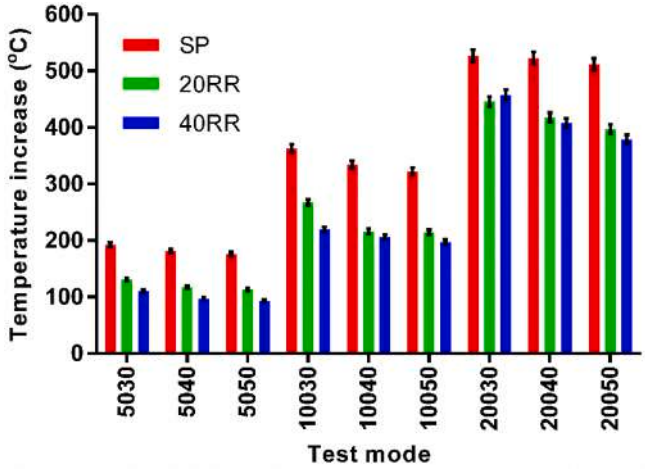

Fig. 14. Temperature increase measurements on the tube front side for the full tests performed on different absorber designs.

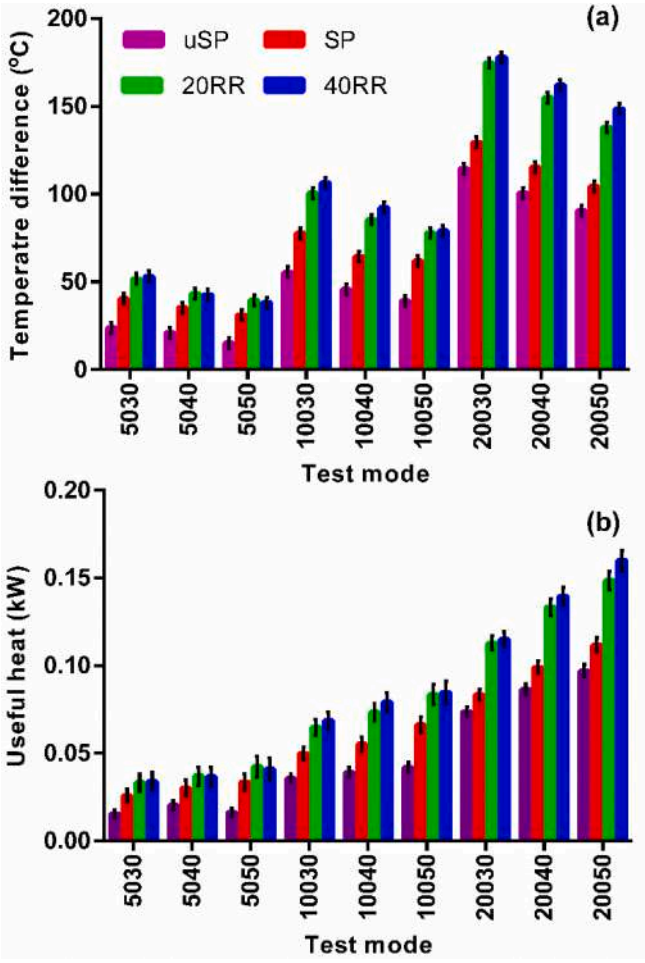

Fig. 15. (a) Air temperature difference achieved during the tests for various absorber configurations, (b) useful heat gained on each sample.

considered in this comparison. According to the graph, as the airflow rate grows, the temperature increase of the hotspots formed on the front side of the tube decreases. Moreover, the integration of the modified tubes is bringing lower peak temperature rise on the heated plate due to the higher heat transfer area between air and tube thanks to the porous structure, where this trend increases as the flux decreases and mass flow increases. The maximum hotspot temperature (T_{hot}) reduction in relative terms was recorded at test 5050 (peak flux = 50 kW/m^2 and m = 50 L/min), in which 40RR and 20RR have lessened the peak temperature rise by respectively 47 and 36%. The enhancement of the cooling in

40RR was higher than 20RR for all the test cases, except test 20030 where 40RR is producing a higher hotspot. The reason for such behavior can be traced back to the slight increase in the solar flux observed at the moment of image capturing in the case of 40RR.

The air temperature differences obtained during the tests are displayed in Fig. 15a, considering the inlet and outlet air temperature sensors. Decreasing the airflow rate at each solar flux increases the temperature difference, as expected from Eq. 7. In the first comparison, when the uSP absorber is the milestone, the application of PYROMARK 2500 coating on the SP has improved the total air temperature increase by an average value of 47%, and a maximum of 105% at test 5050. The porous insertion helps in promoting heat removal and extends the increase in the total temperature increase by an average value of 90 and 95%, having 20 and 40 mm lengths. In order to investigate the mere effect of the porous insert, values of SP were compared to the 20RR and 40RR values. At this stage, it was found that the integration of RR porous blocks could improve the total air temperature difference by 30 and 34%, respectively using 20RR and 40RR. Finally, comparing the values between two modified tubes showed a slightly better behavior of the 40RR, but difficult to quantify in view of the measurement uncertainties.

Fig. 15b illustrates the useful heat generated through each test for different samples. The increase in both the solar flux and airflow rate has improved the total gained heat on all the samples. At each test level, the maximum and minimum heat productions are referring to the 40RR and uSP samples, respectively. As a result, the highest value was achieved as 0.16 kW for the 40RR sample working at test 20050, which reflects a 43% higher gained heat compared to SP. Comparing the values of SP with uSP, it was revealed that as the flux increases, the useful heat improvement decreases, showing that the maximum rise in the useful heat due to the coating application is obtained at the lowest solar flux and the highest flow rate (5050). Although comparing the values of 20RR and 40RR is a little tricky due to the large errors, it is pretty clear that when the solar flux increases, a higher airflow rate with longer porous could increase the amount of useful heat gained by the air.

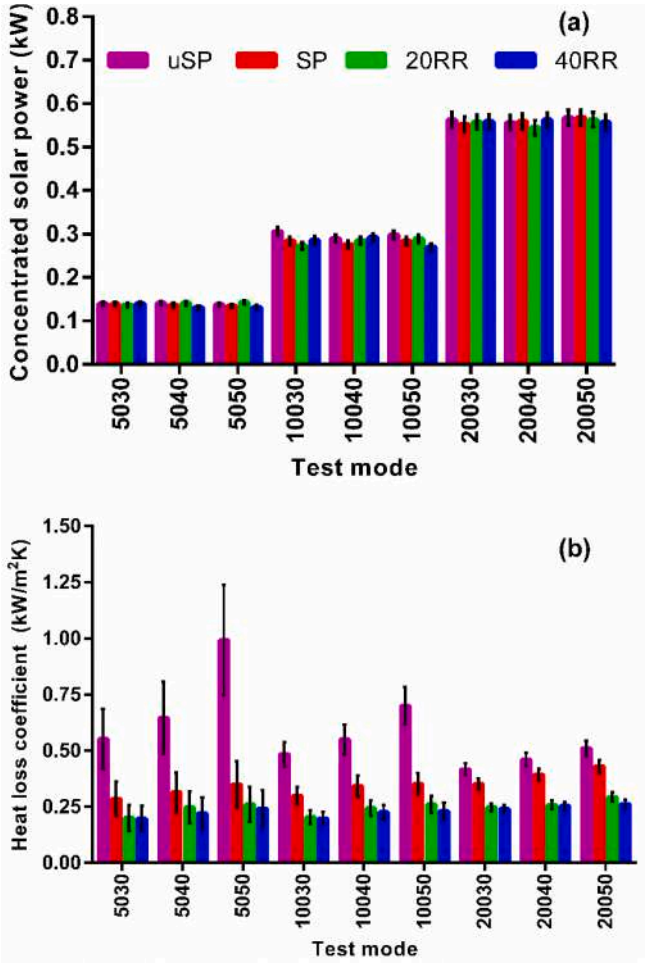

Fig. 16. Comparison of (a) the various solar power irradiated on the samples, (b) U_L through the utilization of different tube designs.

3.2.2. Heat loss effects

The solar power concentrated on the samples is depicted in Fig. 16a, showing that all the concentrated fluxes have been in an acceptable range. Therefore, for the peak fluxes level of 50 kW/m^2, the total power gained by the absorber $E_{(S-Cfocus)}$ lies in 0.13–0.14 kW, while for the peak fluxes of 100 and 200 kW/m^2, the solar powers are 0.27–0.3 kW, and 0.55–0.57 kW.

Fig. 16b provides the evaluation of the heat loss coefficient (U_L), considering different enhancement effects, according to Eq. 8. Based on the measured data, the maximum heat loss coefficients were recorded at uSP, followed by SP, 20RR, and 40RR in all design configurations. Comparing uSP and SP, the absorber coating in SP design could reduce the thermal loss coefficient by an average value of 37%, where the maximum is achieved as 65% at the peak flux of 50 kW/m^2 and an airflow rate of 50 L/min. The analysis of the changing trends showed that the enhancing effects of the coating become significant with the decrease in solar flux and the increase in airflow rate. The reason is that when the coating is applied, the solar absorption increases, which means higher temperature levels will be achieved on the tube wall (see Fig. 11). However, the ability of the plain tube to absorb the heat is limited and if the solar peak flux increases to 200 kW/m^2, the enhancement effect of the coating drops sharply to near 22% (see Fig. 15b). Consider indeed that a higher temperature implies an increase in the heat transfer to the environment, which is the reason behind the lower U_L reduction at high solar peak fluxes. This reflects that the coating is not enough in high flux exposures and highlights the importance of an additional heat-enhancing technique. As also demonstrated in Fig. 15b, the integration of the RR porous increases the total energy gained by the air, reducing the excessive heat on the tube wall and avoiding the sharp increase in heat loss at the highest solar flux. The minimum U_L was also found near 0.2 kW/m^{2}K at the test 5030 for both 20RR and 40RR designs, in which the flux is the lowest and the porous block is inserted.

3.2.3. Energy efficiency

The energy efficiency was also computed for various tube designs to show the thermal performance of each design, as depicted in Fig. 17. According to the results depicted in Fig. 17a, considering the lowest solar flux (50 kW/m^2), the deviations among various efficiency are not very clear due to the large error bars, resulted from the propagation of the measurement uncertainties. Although the increasing trend with coating and porous inserts is clearly visible, the only confident conclusion is that the applications of coating and porous insert could enhance the energy efficiency compared to the uSP sample. The energy efficiency remains constant within the error bars for any given flow rate in each sample. As the solar flux grows to 100 kW/m^2 (Fig. 17b), the significance of differences between the uSP and SP becomes larger, however, it is not enough to distinguish unambiguously the effects of the RR porous integration. In Fig. 17c when the solar flux reaches 200 kW/m^2, the difference between each sample and each level of flow rate grows even more, showing that an increase in the mass flow rate results in an increase in energy efficiency. This could be explained by the higher heat transfer rate between the air and the heated tube for higher flow rates. Analyzing the trend of energy efficiency at this power level and for the airflow rate of 50 L/min revealed that the best thermal performance refers to 40RR with 30% energy efficiency, followed by 26, 20, and 17%, respectively for 20RR, SP, and uSP designs. Moreover, the maximum energy efficiency improvement was obtained as $>$ 120%, with a comparison between uSP and 40RR samples in the test at 100 kW/m^2 and 50

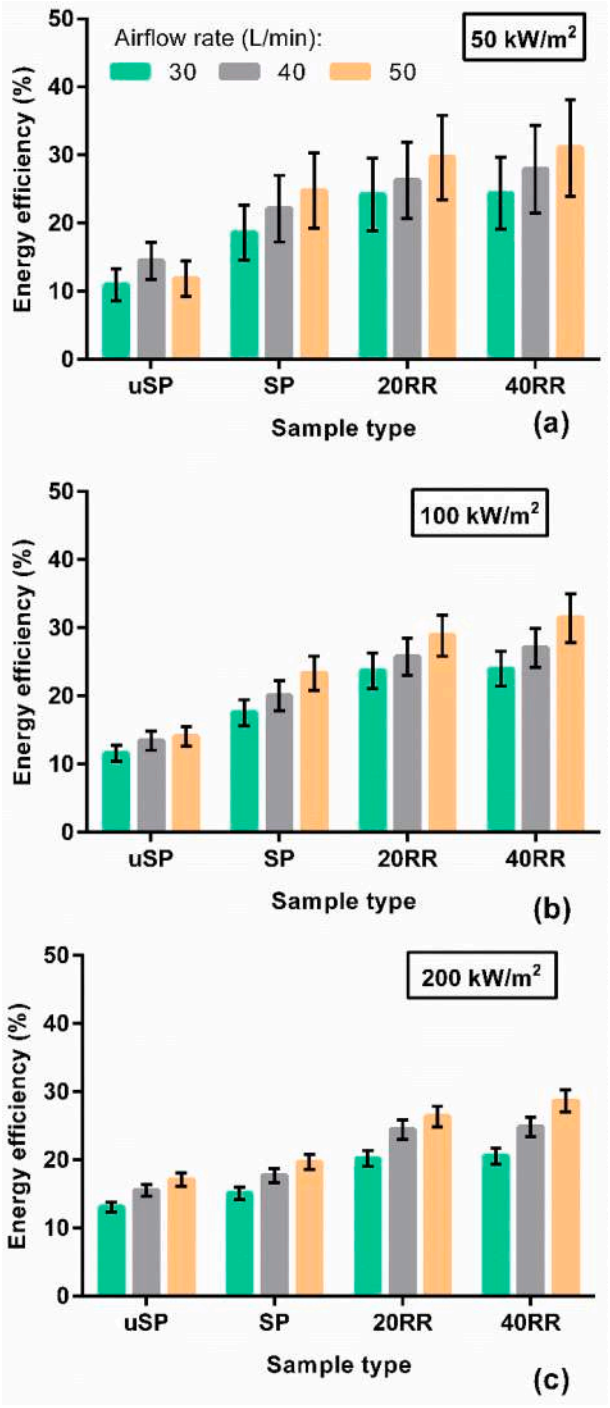

Fig. 17. Energy efficiency variation with different absorber designs computed at peak fluxes of (a) 50 kW/m^2, (b) 100 kW/m^2, (c) 200 kW/m^2.

L/min, followed by an improvement of 45% with a comparison between SP and 40RR sample in the test at 200 kW/m^2 and 50 L/min. Analyzing the effects of the different solar fluxes on the energy efficiency trend does not reflect any special dependency as the efficiency values remain within the uncertainty range at each flow rate and different solar power levels.

To provide a better outlook on the impacts of the RR porous insert, a comparison of the maximum improvement achievements obtained through various enhancement techniques carried out experimentally in a similar context has been presented in Fig. 18. Since a Thermal Enhancement Factor (TEF) accounting for a combination of the gain in

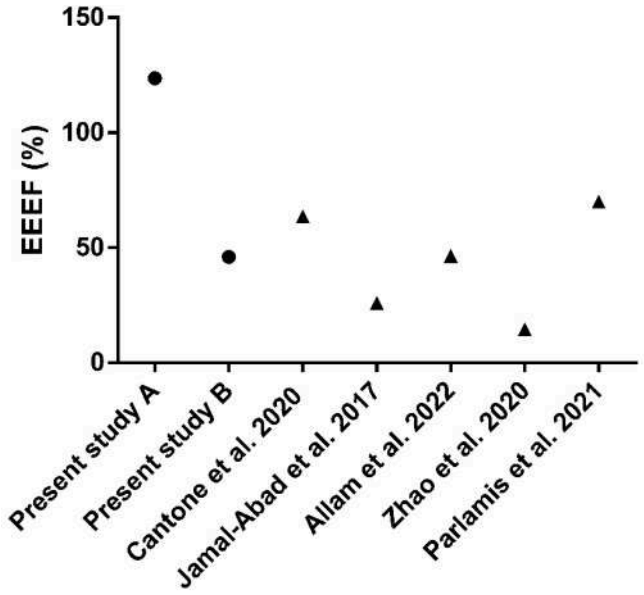

Fig. 18. The Comparison of energy efficiency enhancement found in this study with other research studies.

heat transfer and the loss in pressure drop cannot be computed only base on experimental data, in view of the very different range of airflow rate that could be used to get relevant results in the hydraulic characterization of the different samples with respect to the airflow range adopted for the thermal measurements, we just consider here the gain in energy efficiency. Thus, the EEEF is computed as the growth of the energy efficiency obtained with the modified design with respect to the basic model considered in each study. The maximum EEEF found in this study (Present study A), obtained by the utilization of the 40RR tube over the uSP, outweighs all the similar works. This can be attributed to the hybrid enhancement effect of the PYROMARK coating and the porous insert. If the effect of the RR porous insert is only concerned with comparing the energy efficiency obtained by 40RR over the SP sample, the obtained EEEF (Present study B) stands higher than Jamal-Abad [24], employing the copper foam inside a PTC collector, Allam et al. [49], implementing a helical rotating shaft insert with a tubular PTC absorber and Zhao et al. [50], using a gaseous PTC with pin fin to improve the energy efficiency. However, the EEEF acquired by Cantone et al. [15] for using helical ribs in a gaseous tubular absorber for STP application and Parlamis et al. [51] where a helical-screw tape is employed with a gaseous PTC show slightly an improved performance thanks to their modifications and working conditions.

3.2.4. *Exergy efficiency*

The values of exergy efficiency for various tests and absorber configurations are reported in Fig. 19. The results show that the quality of energy increases with a growth in solar flux, which suggests that the higher the absorber temperature, the higher the exergy efficiency is. The same behavior has also been reported by Kalogirou et al. [52], analyzing a PTC collector. According to Fig. 19a, at the lowest solar flux (50 kW/m^2), unlike the energy efficiency, the improving effects of the coating and porous insert on the exergy efficiency are clear and distinguishable. However, the impact of porous length is still undecidable due to the error bars in 20RR and 40RR. Moreover, at this power level, the effects of various airflow rates are not significant on the exergy efficiency. Fig. 19b shows the same behavior for different absorber designs, working under 100 kW/m^2 solar peak flux. When the solar flux reaches 200 kW/m^2 (in Fig. 18c), the differences between all the samples become meaningful for the flow rate of 50 L/min, showing higher improving effects by 40RR than 20RR. The highest value is found as >

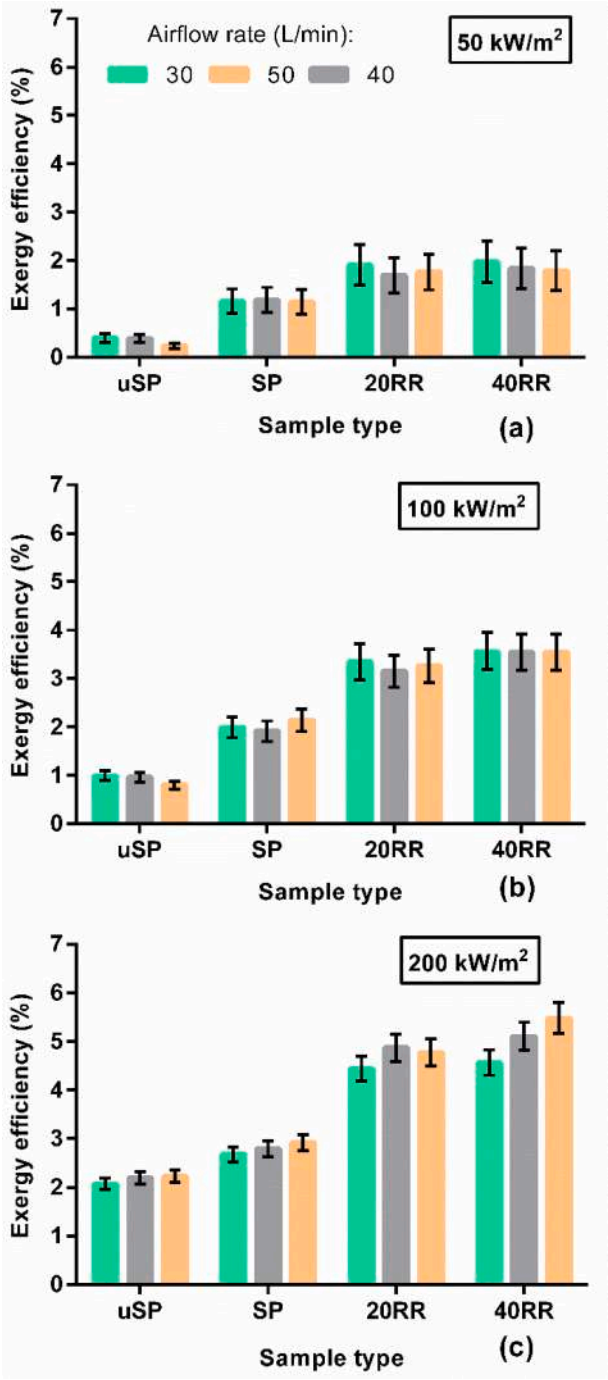

Fig. 19. Exergy efficiency variation with different absorber designs computed at peak fluxes of (a) 50 kW/m^2, (b) 100 kW/m^2, (c) 200 kW/m^2.

5% for 40RR with a flow rate of 50 and solar peak flux of 200 kW/m^2. Comparing the enhancement effects of the porous insert with the SP design, it was found that the average improvement of 20RR and 40RR absorbers are ∽60 and ∽70%, respectively, at the highest flux and highest flow rate. This result demonstrated that the influence of RR porous medium is more evident on the exergy efficiency improvement than energy efficiency.

4. Conclusions and perspective

This work presents an experimental campaign to investigate the impacts of a novel porous medium made of tiny copper Raschig Rings for a solar furnace test facility, located at Plataforma Solar de Almería, Spain. Experiments were designed to include the assessment of four absorber designs, including uSP; a conventional absorber tube with no surface coating, SP; a conventional absorber tube treated with the coating, 20RR; a tube with 20 mm RR porous insert and coating, 40RR; a tube with 40 mm RR porous insert and coating. The main findings of the hydraulic and thermal evaluations are presented below;

- Adiabatic hydraulic tests proved that the integration of the porous medium requires a higher pumping power, where the maximum pressure drop increase was measured at the highest flow rate (800 L/min) with relatively ∼ 2.5 times and ∼ 4 times for the 20RR and 20RR samples, respectively with respect to the SP tubes. The pressure gradient within the RR dominates the pressure drop and is comparable in the two RR samples, with only marginal effects of the minor losses at the beginning and end of the porous blocks.
- The Darcy–Dupuit–Forchheimer model turns out to be very well suited to reproduce the pressure drop in the porous inserts.
- Inserting the porous medium in the center of the concentrated flux (peak load area) turns the hottest point in the SP model into the coolest point in the 20RR and 40RR models. Moreover, extending the porous length increases the cool area on the heated side, also providing a stronger thermal mixing and resulting in lower tube wall temperature and higher air temperature difference.
- Applying the PYROMARK 2500 coating on the SP improves the air temperature increase by almost 50% at the highest heat flux. The integration of 20 mm and 40 mm porous inserts could also bring further improvements to the total air temperature increase by>30% using 20RR and 40RR.
- The determination of U_L suggested that the application of the coating and the integration of RR porous could be a solution to reduce the total thermal loss coefficient to 0.25 kW/m^{2}K.
- The energy and exergy analyses revealed that the effects of various flow rates on both efficiencies are not significant. Different levels of solar flux could only change the exergy efficiency with a certain confidence level, where increasing the solar flux level rises the exergy efficiency. Furthermore, the results demonstrated that using the RR porous inserts could increase the energy efficiency to 30% and 25% for 40RR and 20RR samples. Considering the exergy efficiency, the 40RR design was able to bring > 10% further improvement to the 20RR design, reaching > 70% augmentation factor than the SP design.

During the present study, the applicability of RR porous media for performance augmentation in tubular air-based point-focusing solar systems was proved in terms of energy and exergy efficiencies. Note, however, that a Key Performance Indicator (KPI) such as a TEF, weighting somehow the increase in heat transfer with respect to the smooth pipe with the increase of the pressure drop, was not computed here in view of the different flow test ranges needed for the hydraulic and thermal tests. In the development pathway of the technology presented here, the experimental data analyzed in this study, will be used to validate the most suitable CFD model, following by the determination of the TEF. Based on that, further optimizations and enhancement of the receiver performance will be possible.

CRediT authorship contribution statement

Hossein Ebadi: Conceptualization, Methodology, Formal analysis, Validation, Visualization, Writing – original draft. **Antonio Cammi:** Conceptualization, Methodology, Writing – review & editing. **Rosa Difonzo:** Methodology, Investigation. **José Rodríguez:** Investigation. **Laura Savoldi:** Conceptualization, Resources, Methodology, Writing – review & editing, Supervision.

Declaration of Competing Interest

The authors declare that they have no known competing financial interests or personal relationships that could have appeared to influence the work reported in this paper.

Data availability

Data will be made available on request.

Acknowledgements

The tests have been financed by the European Union Horizon 2020 project funded under the Research Infrastructure Programme SFERA III: Solar Facilities for the European Research Area – Third Phase, under grant agreement N. 823802. The authors also acknowledge Dr. A. Leggieri from THALES for the support in manufacturing the samples and Mr. J. Galindo from PSA for assistance in performing the experimental tests.

References:

[1] IRENA, Global Renewables Outlook: Energy transformation 2050. 2020.
[2] I. Renewable Energy Agency, "RENEWABLE CAPACITY STATISTICS 2022," 2022. [Online]. Available: www.irena.org.
[3] Achkari O, El Fadar A. Latest developments on TES and CSP technologies – Energy and environmental issues, applications and research trends. Appl Therm Eng 2020; 167:114806. https://doi.org/10.1016/j.applthermaleng.2019.114806.
[4] Merchán RP, Santos MJ, Medina A, Calvo Hernández A. High temperature central tower plants for concentrated solar power: 2021 overview. Renew Sustain Energy Rev 2022;155:111828. https://doi.org/10.1016/j.rser.2021.111828.
[5] Boerema N, Morrison G, Taylor R, Rosengarten G. High temperature solar thermal central-receiver billboard design. Sol Energy 2013;97:356–68. https://doi.org/10.1016/j.solener.2013.09.008.
[6] Benoit H, Spreafico L, Gauthier D, Flamant G. Review of heat transfer fluids in tube-receivers used in concentrating solar thermal systems: Properties and heat transfer coefficients. Renew Sustain Energy Rev 2016;55:298–315. https://doi.org/10.1016/j.rser.2015.10.059.
[7] Vutukuru R, Pegallapati AS, Maddali R. Suitability of various heat transfer fluids for high temperature solar thermal systems. Appl Therm Eng 2019;vol. 159: 113973. https://doi.org/10.1016/j.applthermaleng.2019.113973.
[8] Bellos E, Tzivanidis C, Antonopoulos KA. A detailed working fluid investigation for solar parabolic trough collectors. Appl Therm Eng 2017;114:374–86. https://doi.org/10.1016/j.applthermaleng.2016.11.201.
[9] Ávila-Marín AL. Volumetric receivers in Solar Thermal Power Plants with Central Receiver System technology: A review. Sol Energy 2011;85(5):891–910. https://doi.org/10.1016/j.solener.2011.02.002.
[10] Neber M, Lee H. Design of a high temperature cavity receiver for residential scale concentrated solar power. Energy 2012;47(1):481–7. https://doi.org/10.1016/j.energy.2012.09.005.
[11] Cagnoli M, Froio A, Savoldi L, Zanino R. Multi-scale modular analysis of open volumetric receivers for central tower CSP systems. Sol Energy 2019;190(July): 195–211. https://doi.org/10.1016/j.solener.2019.07.076.
[12] Chen Y, Wang D, Zou C, Gao W, Zhang Y. Thermal performance and thermal stress analysis of a supercritical CO2 solar conical receiver under different flow directions. Energy 2022;246:123344. https://doi.org/10.1016/j.energy.2022.123344.
[13] Cagnoli M, Savoldi L, Zanino R, Zaversky F. Coupled optical and CFD parametric analysis of an open volumetric air receiver of honeycomb type for central tower CSP plants. Sol Energy 2017;155:523–36. https://doi.org/10.1016/j.solener.2017.06.038.
[14] Gorjian S, Ebadi H, Calise F, Shukla A, Ingrao C. A review on recent advancements in performance enhancement techniques for low-temperature solar collectors. Energy Convers Manag Oct. 2020;222:113246. https://doi.org/10.1016/j.enconman.2020.113246.
[15] Cantone M, Cagnoli M, Fernandez Reche J, Savoldi L. One-side heating test and modeling of tubular receivers equipped with turbulence promoters for solar tower applications. Appl Energy 2020;277:115519. https://doi.org/10.1016/j.apenergy.2020.115519.
[16] Ahmed KA, Natarajan E. Numerical investigation on the effect of toroidal rings in a parabolic trough receiver with the operation of gases: An energy and exergy analysis. Energy 2020;203:117880. https://doi.org/10.1016/j.energy.2020.117880.
[17] Bellos E, Tzivanidis C, Daniil I, Antonopoulos KA. The impact of internal longitudinal fins in parabolic trough collectors operating with gases. Energy Convers Manag 2017;135:35–54. https://doi.org/10.1016/j.enconman.2016.12.057.
[18] Nemś M, Kasperski J. Experimental investigation of concentrated solar air-heater with internal multiple-fin array. Renew Energy 2016;97:722–30. https://doi.org/10.1016/j.renene.2016.06.038.
[19] Kasperski J, Nemś M. Investigation of thermo-hydraulic performance of concentrated solar air-heater with internal multiple-fin array. Appl Therm Eng 2013;58(1):411–9. https://doi.org/10.1016/j.applthermaleng.2013.04.018.
[20] Reddy KS, Satyanarayana GV. Numerical Study of Porous Finned Receiver for Solar Parabolic Trough Concentrator. Eng Appl Comput Fluid Mech Jan. 2008;2(2): 172–84. https://doi.org/10.1080/19942060.2008.11015219.
[21] Ravi Kumar K, Reddy KS. Effect of porous disc receiver configurations on performance of solar parabolic trough concentrator. Heat Mass Transf 2012;48(3): 555–71. https://doi.org/10.1007/s00231-011-0903-8.
[22] Reddy KS, Ravi Kumar K, Ajay CS. Experimental investigation of porous disc enhanced receiver for solar parabolic trough collector. Renew Energy 2015;77: 308–19. https://doi.org/10.1016/j.renene.2014.12.016.
[23] Zheng Z-J, Li M-J, He Y-L. Thermal analysis of solar central receiver tube with porous inserts and non-uniform heat flux. Appl Energy 2017;185:1152–61. https://doi.org/10.1016/j.apenergy.2015.11.039.
[24] Jamal-Abad MT, Saedodin S, Aminy M. Experimental investigation on a solar parabolic trough collector for absorber tube filled with porous media. Renew Energy 2017;107:156–63. https://doi.org/10.1016/j.renene.2017.02.004.
[25] Mund C, Rathore SK, Sahoo RK. A review of solar air collectors about various modifications for performance enhancement. Sol Energy 2021;228:140–67. https://doi.org/10.1016/j.solener.2021.08.040.
[26] Chamoli S, Chauhan R, Thakur NS, Saini JS. A review of the performance of double pass solar air heater. Renew Sustain Energy Rev 2012;16(1):481–92. https://doi.org/10.1016/j.rser.2011.08.012.
[27] Rashidi S, Esfahani JA, Rashidi A. A review on the applications of porous materials in solar energy systems. Renew Sustain Energy Rev 2017;73:1198–210. https://doi.org/10.1016/j.rser.2017.02.028.
[28] Jamal-Abad MT, Saedodin S, Aminy M. Heat transfer in concentrated solar air-heaters filled with a porous medium with radiation effects: A perturbation solution. Renew Energy 2016;91:147–54. https://doi.org/10.1016/j.renene.2016.01.050.
[29] Savoldi L, Allio A, Bovento A, Cantone M, Fernandez Reche J. Experimental and numerical investigation of a porous receiver equipped with Raschig Rings for CSP applications. Sol Energy 2020.
[30] Schultes M. Raschig Super-Ring: A New Fourth Generation Packing Offers New Advantages. Chem Eng Res Des 2003;81(1):48–57. https://doi.org/10.1205/026387603321158186.
[31] Savoldi L, Avramidis KA, Albajar F, Alberti S, Leggieri A, Sanchez F. A Validation Roadmap of Multi-Physics Simulators of the Resonator of MW-Class CW Gyrotrons for Fusion Applications. Energies 2021;14(23):pp. https://doi.org/10.3390/en14238027.
[32] Moghaddam EM, Foumeny EA, Stankiewicz AI, Padding JT. Heat transfer from wall to dense packing structures of spheres, cylinders and Raschig rings. Chem Eng J 2021;407:127994. https://doi.org/10.1016/j.cej.2020.127994.
[33] Moyse B. Raschig ring HDS catalysts reduce pressure drop. vol. 82:53; 1984.
[34] Ebadi H, Allio A, Cammi A, Savoldi L. First numerical evaluation of the thermal performance of a tubular receiver equipped with Raschig rings for CSP applications; 2021. https://doi.org/10.1115/POWER2021-65714.
[35] Allio A, Difonzo R, Leggieri A, Legrand F, Marchesin R, Savoldi L. Test and modeling of the hydraulic performance of high-efficiency cooling configurations for gyrotron resonance cavities. Energies 2020;13(5):pp. https://doi.org/10.3390/en13051163.
[36] Boubault A, Ho CK, Hall A, Lambert TN, Ambrosini A. Durability of solar absorber coatings and their cost-effectiveness. Sol Energy Mater Sol Cells 2017;166:176–84. https://doi.org/10.1016/j.solmat.2017.03.010.
[37] Roldán MI, Monterreal R. Heat flux and temperature prediction on a volumetric receiver installed in a solar furnace. Appl Energy 2014;120:65–74. https://doi.org/10.1016/j.apenergy.2014.01.029.
[38] Ho CK, Mahoney AR, Ambrosini A, Bencomo M, Hall A, Lambert TN. Characterization of Pyromark 2500 for High-Temperature Solar Receivers. pp. 509–518, Jul. 23, 2012, doi: https://doi.org/10.1115/ES2012-91374.
[39] Hahm T, Schmidt-Traub H, Leßmann B. A cone concentrator for high-temperature solar cavity-receivers. Sol Energy 1999;65(1):33–41. https://doi.org/10.1016/S0038-092X(98)00119-4.
[40] Noglik A, Roeb M, Sattler C, Pitz-Paal R. Modeling of a solar receiver–reactor for sulfur-based thermochemical cycles for hydrogen generation. Int J Energy Res Apr. 2011;35(5):449–58. https://doi.org/10.1002/er.1707.
[41] Li B, Oliveira FAC, Rodríguez J, Fernandes JC, Rosa LG. Numerical and experimental study on improving temperature uniformity of solar furnaces for materials processing. Sol Energy 2015;115:95–108. https://doi.org/10.1016/j.solener.2015.02.023.
[42] Rodriguez J, Galindo J, Cañadas I, Monterreal R, Fernandez-Reche J. Design and Characterization of the New FAHEX 100 Concentrator of PSA's SF60 Solar Furnace; 2022.
[43] Zhu J, et al. Experimental study of the energy and exergy performance for a pressurized volumetric solar receiver. Appl Therm Eng 2016;104:212–21. https://doi.org/10.1016/j.applthermaleng.2016.05.075.
[44] Petela R. Exergy of undiluted thermal radiation. Sol Energy 2003;74(6):469–88. https://doi.org/10.1016/S0038-092X(03)00226-3.
[45] J. P. (Jack P. Holman, Experimental methods for engineers. McGraw-Hill/Connect Learn Succeed; 2012.
[46] Otaru AJ. Review on processing and fluid transport in porous metals with a focus on bottleneck structures. Met Mater Int 2020;26(4):510–25. https://doi.org/10.1007/s12540-019-00345-9.
[47] Nowak R. Estimation of viscous and inertial resistance coefficients for various heat sink configurations. Procedia Eng 2016;157:122–30. https://doi.org/10.1016/j.proeng.2016.08.347.

[48] Difonzo R, Allio A, Leggieri A, Savoldi L. Validation of the CFD model of a Gyrotron cavity cooling system through the Multivariate Metric approach; 2020.
[49] Allam M, Tawfik M, Bekheit M, El-Negiry E. Experimental investigation on performance enhancement of parabolic trough concentrator with helical rotating shaft insert. Sustainability 2022;14(22):pp. https://doi.org/10.3390/su142214667.
[50] Zhao Z, Bai F, Zhang X, Wang Z. Experimental study of pin finned receiver tubes for a parabolic trough solar air collector. Sol Energy 2020;207:91–102. https://doi.org/10.1016/j.solener.2020.06.070.
[51] Parlamış H, Özden E, Büker MS. Experimental performance analysis of a parabolic trough solar air collector with helical-screw tape insert: A comparative study. Sustain Energy Technol Assessments 2021;47:101562. https://doi.org/10.1016/j.seta.2021.101562.
[52] Kalogirou SA, Karellas S, Braimakis K, Stanciu C, Badescu V. Exergy analysis of solar thermal collectors and processes. Prog Energy Combust Sci 2016;56:106–37. https://doi.org/10.1016/j.pecs.2016.05.002.